Effects of inertia and stratification in incompressible ideal fluids: pressure imbalances by rigid confinement

Effects of inertia and stratification in incompressible ideal fluids: pressure imbalances by rigid confinement

R. Camassa [1], S. Chen[1], G. Falqui[2], G. Ortenzi[2] and M. Pedroni [3]

[1]Carolina Center for Interdisciplinary Applied Mathematics, Department of Mathematics, University of North Carolina, Chapel Hill, NC 27599, USA

[2]Dipartimento di Matematica e Applicazioni, Università di Milano-Bicocca, Milano, Italy

[3]Dipartimento di Ingegneria, Università di Bergamo, Dalmine (BG), Italy

Abstract

Consequences of density stratification are studied for an ideal (Euler) incompressible fluid, confined to move under gravity between rigid lids but otherwise free to move along horizontal directions. Initial conditions that generate horizontal pressure imbalances in a laterally unbounded domain are examined. The aim is to show analytically the existence of classes of initial data for which total horizontal momentum evolves in time, even though only vertical forces act on the fluid in this set-up. A simple class of such initial conditions, leading to momentum evolution, is identified by systematic asymptotic expansions of the governing inhomogeneous Euler equations in the small density variation limit. These results for Euler equations are compared and confirmed with long-wave asymptotic models, which can handle arbitrary density variations and provide closed-form mathematical expressions for limiting cases. In particular, the role of wave-dispersion arising from the fluid's inertia is captured by the long-wave models, even for short time dynamics emanating from initial conditions outside the models' asymptotic range of validity. These results are compared with direct numerical simulations for variable density Euler fluids, which further validate the numerical algorithms and the analysis.

1 Introduction

This paper deals with some specific aspects of the theory of stratified ideal incompressible fluids, rigidly confined in (two-dimensional) infinite horizontal-slab domains. Though highly idealized, this set-up nonetheless offers the simplest setting which can capture the kind of subtle effects sometimes masked in more complex situations. In a previous paper (Camassa et al. 2012) we isolated and studied a phenomenon which to the best of our knowledge has not received much attention in the current literature: horizontal momentum conservation can be violated in the dynamics of a fluid in the above configuration. This violation can be viewed as surprising, as the only acting body-force field is the vertical gravity and the fluid is free to move laterally. Possibly the first mention of this peculiar feature of stratified fluid dynamics can be traced back to Benjamin (1986), in his investigation of the Hamiltonian formalism for inviscid incompressible fluids. Despite the relatively long time elapsed, it appears that Benjamin's observation about (in his own words) "this curious fact" have been largely ignored since.

In the horizontal slab set-up, whenever hydrostatic conditions apply at infinity, this violation of momentum conservation is proportional (up to terms that arise from possibly different configurations at $x = \pm\infty$) to the difference of the layer-averaged pressure at the far ends of the channel. As we will see, this pressure imbalance enters another physically interesting quantity, namely the (total) vorticity of the system. Admittedly, the effects herewith considered can be viewed as small, because the violation of momentum conservation must necessarily be a vanishing function of the difference ρ_Δ of the density range of the fluid as this goes to zero (momentum conservation recovers in the limit of a homogeneous fluid). Small density variations are common to many applications such as geophysics, however the large scales often involved in such applications justify considering the idealized set-up of laterally infinite fluids and might lead to non-negligible cumulative effects,

even when these are small over local scales. Of course, the implications arising from considering rigid lids upper constraints in these applications remain to be seen; however, this limiting case may be relevant for establishing a comprehensive framework in which the dynamics of the incompressible limit for density-stratified fluids can be properly interpreted.

We shall mainly deal with incompressible, inviscid two-layer (Euler) fluids of constant different densities $\rho_2 > \rho_1$, separated by an interface located at $z = \eta(x,t)$ (not necessarily smooth), where (x,z) are horizontal and vertical Cartesian coordinates in the plane. This choice is convenient for analytical purposes, and while numerically challenging, it can nonetheless be implemented in direct simulations of stratified Euler flows. While restrictive, the two-layer assumption can be representative of the dynamics of Euler fluids with smooth density variations as well (see, e.g., Camassa et al. 2006, Camassa & Tiron 2011). In particular, for two-layer fluids in which the interface height is the same at $\pm\infty$, the pressure imbalance $P_{\Delta} \equiv \lim_{x\to+\infty} p(x,\eta(x,t)) - \lim_{x\to-\infty} p(x,\eta(x,t))$ is equal to the difference of the pressures $p(\pm\infty, z_0)$ for any reference height z_0, as it could be obtained from Benjamin (1986) for smooth stratifications.

Our main focus will be on initial conditions with *null* velocity and small $\rho_{\Delta} \equiv \rho_2 - \rho_1$. This choice, as shown below, restricts the effects on the pressure imbalance of stratification at initial times to order ρ_{Δ}^2, as opposed to order ρ_{Δ}, as it might be expected at first. However, besides being simpler to implement numerically, this choice has the advantage of leading to closed form formulae, and identifies from a theoretical viewpoint a significant class of interface profile configurations giving rise to pressure imbalance. In turn, these correspond to horizontal momentum non-preserving time evolutions. In particular, the setting of zero-velocity configurations will be instrumental in Section 4, where we shall adopt a perturbative point of view (in the limit $\rho_{\Delta} \to 0$) to solve the elliptic equations which determine the pressure at $t = 0$. Some compact expressions for the pressure imbalances can then be obtained. Our analysis will be carried out directly on the Euler equations of motion in two dimensions; however, as a kind of benchmark for testing ideas, we shall also consider long-wave one-dimensional reductions of our two-dimensional set-up, such as the strongly nonlinear model introduced in Choi & Camassa (1999), for the description of strongly nonlinear internal waves in two-fluid systems. We will also briefly review the Lagrangian and Hamiltonian formalism of the Euler equations, in particular adapting it to the two-fluid configuration, which allows the framework of conservation laws to be established from a more general standpoint.

More specifically, the layout of the paper is as follows. In Section 2 we shall review the set-up of our physical system within the Euler formalism, and, in particular, focus on the relation between non-conservation of horizontal momentum and the pressure imbalance P_{Δ} established in Camassa et al. (2012). Section 2.2 describes the asymptotic behaviour of P_{Δ} with respect to the small ρ_{Δ} expansion. In particular, we establish that this behaviour is linear for generic initial configurations with nonzero initial velocities, while it becomes *quadratic* when static initial conditions are considered. The relation between the time derivative of the total vorticity and the pressure imbalance is derived, both in the smooth and the two-layer stratification, in Section 2.3. In Section 3 we use strongly nonlinear models to derive predictions about the pressure imbalances. The analytical and numerical fidelity of the models to the parent Euler system is tested on special configurations for zero-velocity initial data. It is worthwhile to remark that, in the zero-velocity case, the dispersionless limit of the long-wave model fails to provide the correct predictions for the pressure imbalance P_{Δ}. Accuracy can be restored by including the first order dispersive correction of the model as introduced in Choi & Camassa (1999).

Next, in Section 4 we discuss pressure imbalances with zero-velocity initial data for two-layer fluids. The exact problem of solving the Laplace equation for the initial pressure can be viewed as a form of Neumann-to-Dirichlet problem for a (two-layer) strip. We adopt a simple perturbative approach in the limit of small density difference ρ_{Δ}, turning this problem into an iterative family of Poisson equations which allow for a closed-form integral expression for the second order term $P_{\Delta}^{(2)}$ of the pressure imbalance associated with any interface profile $z = \eta(x)$. In some cases (e.g., piecewise linear profiles) this expression easily yields explicit formulae for $P_{\Delta}^{(2)}$ (which in suitable limits are expressed by Bernoulli-like polynomials). A sample of these formulae and their interpretation is contained in Section 4.3 and Section 4.4. In particular, within a certain class of initial data, we determine the configuration that maximizes the pressure imbalance. In Section 5 the

dam-break configuration is studied. At $t = 0$ an exact explicit value for $\langle p \rangle_{\Delta}$ can be obtained. The comparison of the theoretical results with full-Euler numerical experiments, in Section 6, further illustrates the (short-time) dynamics arising from these pressure imbalances of these configurations and its effects on the horizontal momentum. Computations are performed with the VARDEN algorithm (Almgren et al. 1998) which solves the inhomogeneous Euler equations. The two-layer (sharp interface) set-up can be viewed as a severe test for the code, which gets validated by the overall good agreement with the analytical results. In Section 7 we discuss our findings and point to future work.

We have also provided additional information in appendices. Specifically, Appendix A is devoted to reconcile the apparent paradox of lack of momentum conservation with the self-evident translational symmetry of the systems we study. Appendix B discusses some technical points on the time evolutions of these systems. Appendix C briefly examines the limiting case of "air-water" systems, in which one of the densities goes to zero. Non-trivial boundary effects on the pressure imbalance which are masked by the opposite near-density limit emerge in this case, due to the interface profile touching the channel plates along some intervals.

2 The physical system and its governing equations

We study the Euler equations for an ideal incompressible and inhomogeneous fluid subject to gravity,

$$\mathbf{v}_t + \mathbf{v} \cdot \nabla \mathbf{v} = -\frac{\nabla p}{\rho} - g\mathbf{k}\,, \qquad \nabla \cdot \mathbf{v} = 0\,, \qquad \rho_t + \mathbf{v} \cdot \nabla \rho = 0\,. \tag{1}$$

Here $\mathbf{v} = (u, v, w)$ is the velocity field with respect to Cartesian coordinates (x, y, z) oriented by unit vectors $(\mathbf{i}, \mathbf{j}, \mathbf{k})$, with $\mathbf{k}$ directed vertically upwards, ρ and p are the density and pressure fields, respectively, and g is the constant gravity acceleration; all physical variables depend on spatial coordinates and time t. Besides their well known theoretical interest, this set of equations can be viewed as governing the motion of real fluids with sufficient accuracy whenever viscosity, compressibility and diffusivity effects can be considered small during the time evolution. In particular, the fluid domains we shall consider here are slabs in the (x, z) plane rigidly confined by horizontal "plates" of infinite extent located at $z = z_{\text{bottom}} \equiv 0$ and $z = z_{\text{top}} \equiv h$. Our study will mainly focus on two dimensional y-independent dynamics, though it can be generalized to fully three dimensional cases. The Euler equations (1) are supplemented by the boundary conditions:

$$\mathbf{v}(x, \cdot) \to 0 \quad \text{for } |x| \to \infty, \quad w(x, 0) = w(x, h) = 0, \tag{2}$$

with the fluid at the far ends of the channel in hydrostatic equilibrium,

$$\frac{\partial p}{\partial z} = -g\rho, \quad |x| \to \infty. \tag{3}$$

2.1 Pressure imbalances and horizontal momentum

Consider the Euler equations for the horizontal component of the fluid's momentum

$$(\rho u)_t = -u(\rho u)_x - w(\rho u)_z - p_x\,. \tag{4}$$

Assuming a smooth stratification and integrating this equation on the strip $\mathcal{S} = \mathbb{R} \times [0, h]$ yields the time variation of the horizontal component Π_1 of the total momentum

$$\begin{aligned} \frac{d}{dt}\Pi_1 &= \int_{\mathcal{S}} (\rho u)_t \, \mathrm{d}A = -\int_{\mathcal{S}} \left((\rho u^2)_x + (\rho u w)_z - \rho u (u_x + w_z) + p_x \right) \mathrm{d}A \\ &= -\int_0^h \left(\int_{\mathbb{R}} (\rho u^2 + p)_x \, \mathrm{d}x \right) \mathrm{d}z = -h(\langle p(+\infty) \rangle - \langle p(-\infty) \rangle), \end{aligned} \tag{5}$$

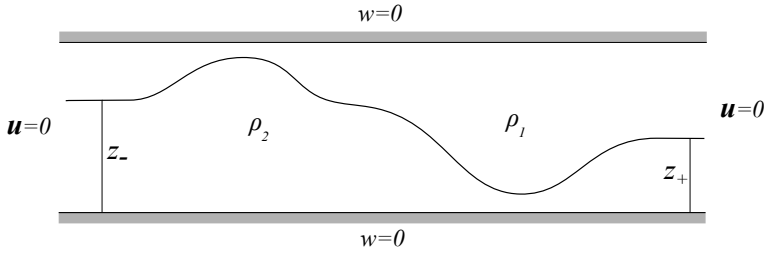

Figure 1: A two-layer configuration with different asymptotic heights.

where we used incompressibility and the asymptotic hydrostatic conditions (see also Benjamin 1986). Hereafter the symbol $\langle f \rangle$ stands for the (total) vertical channel average,

$$\langle f(\cdot) \rangle \equiv \frac{1}{h} \int_0^h f(\cdot, z)\, \mathrm{d}z.$$

2.1.1 The two-layer case

A curious consequence on the nonconservation of linear momentum due to the interplay between fluid's inertia, incompressibility and stratification has been studied in Camassa et al. (2012) for a two-layer incompressible inviscid fluid. For completeness, here we summarize (with minor notational differences) the main results therein.

The dynamics of an inviscid and incompressible fluid stratified in layers of uniform density ρ_j is governed by the Euler equations for the velocity components (u_j, w_j) and the pressure p_j, for each of the layers; in two dimensional Cartesian coordinates (x, z):

$$u_{j\,x} + w_{j\,z} = 0 \tag{6}$$

$$u_{j\,t} + u_j u_{j\,x} + w_j u_{j\,z} = -p_{j\,x}/\rho_j \tag{7}$$

$$w_{j\,t} + u_j w_{j\,x} + w_j w_{j\,z} = -p_{j\,z}/\rho_j - g. \tag{8}$$

For a two-layer fluid, $j = 1$ ($j = 2$) will stand for the upper (lower) fluid, respectively, and $\rho_1 \le \rho_2$ must be assumed for stable stratification (see figure 1 for a sketch of this set-up). The boundary conditions at the interface $z = \eta(x, t)$ are the continuity of normal velocity and pressure

$$\eta_t + u_1 \eta_x = w_1, \quad \eta_t + u_2 \eta_x = w_2, \quad p_1 = p_2 \equiv P \qquad \text{at} \quad z = \eta(x, t), \tag{9}$$

where $P(x, t)$ denotes the interfacial pressure. Let us rewrite the Euler system (8) in terms of layer-averages (see, e.g., Wu (1981) and Camassa & Levermore (1997)). (For a smoothly stratified fluid, this is equivalent to singling out an intermediate level set of constant density $z = \eta(x, t)$ and carrying similar manipulations since such a set will always be a material surface.) Layer-mean quantities $\bar{f}$ are defined by

$$\bar{f}_j(x, t) \equiv \frac{1}{\eta_j} \int_{[\eta_j]} f(x, z, t)\, \mathrm{d}z\,, \tag{10}$$

where η_j are the layer-thicknesses (i.e., $\eta_1 = h - \eta$ and $\eta_2 = \eta$) and the intervals of integration $[\eta_j]$ are $z \in (\eta, h)$ for the upper- and $z \in (0, \eta)$ for the lower-layer, respectively. With this notation, integration (6)–(7) across the layers with the boundary conditions (2) and (9) yields the layer-mean equations for the upper (lower) fluid

$$\eta_{j\,t} + \big(\eta_j \overline{u}_j\big)_x = 0 \tag{11}$$

$$\rho_j (\eta_j \overline{u}_j)_t + \rho_j \big(\eta_j \overline{u_j u_j}\big)_x = -(\eta_j \overline{p_j})_x + (-1)^j \eta_x P\,, \qquad j = 1, 2\,. \tag{12}$$

Layer averages are just a local version of the integral form of the horizontal momentum balance for each layer, which can be expressed for a section of the channel by integrating equations (12) over some x-interval

$L_- \le x \le L_+$. The horizontal momentum balances of the upper ($j = 1$) and lower ($j = 2$) layer for this section are, respectively,

$$\frac{d\Pi_{1j}^{\ell}}{dt} \equiv \frac{d}{dt}\int_{L_-}^{L_+} \rho_j \eta_j \overline{u}_j \,\mathrm{d}x + \rho_j \eta_j \overline{u_j u_j}|_{L_-}^{L_+} = -\,\eta_j \overline{p_j}|_{L_-}^{L_+} + (-1)^j \int_{L_-}^{L_+} \eta_x P \,\mathrm{d}x\,, \tag{13}$$

since neither the pressure at the rigid horizontal surfaces nor the external gravity field contribute horizontal components of forces. Taking into account that

$$\sum_{j=1}^{2} \eta_j \overline{p_j}|_{L_-}^{L_+} = h(\langle p(L_+)\rangle - \langle p(L_-)\rangle),$$

and that the total horizontal momentum of the two-fluid's system is the sum of the contributions of the individual layers, in the limit $L_\pm \to \pm\infty$ (e.g., $L_\pm = \pm L$) and $\Pi_1^{\ell} \to \Pi_1$, system (13) yields the two-layer analogue of Equation (5), i.e.,

$$\frac{d\Pi_1}{dt} = \frac{d\Pi_{11}}{dt} + \frac{d\Pi_{12}}{dt} = -h\langle p\rangle_{\Delta}\,, \tag{14}$$

where $\langle p\rangle_{\Delta} \equiv \langle p(+\infty)\rangle - \langle p(-\infty)\rangle$. In hydrostatic equilibrium the layer-mean pressures are

$$\overline{p_j} = (-1)^j g\rho_j \frac{\eta_j}{2} + P\,, \quad j = 1, 2\,. \tag{15}$$

Taking this into account at $\pm\infty$, we get

$$\frac{d\Pi_1}{dt} = \frac{d\Pi_{11}}{dt} + \frac{d\Pi_{12}}{dt} = -hP_{\Delta} - \frac{1}{2}\rho_{\Delta} g(z_+^2 - z_-^2) - \rho_1 gh(z_+ - z_-), \tag{16}$$

where $P_{\Delta} \equiv \lim_{x\to+\infty} p(x, \eta(x,t)) - \lim_{x\to-\infty} p(x, \eta(x,t))$,

$$z_- \equiv \lim_{x\to-\infty} \eta(x,t), \quad z_+ \equiv \lim_{x\to+\infty} \eta(x,t), \quad \text{for all } t, \tag{17}$$

and $\rho_{\Delta} = \rho_2 - \rho_1$. In particular, by comparing (14) and (16), we have

$$\langle p\rangle_{\Delta} = P_{\Delta} + \frac{\rho_{\Delta} g}{2h}(z_+^2 - z_-^2) + \rho_1 g(z_+ - z_-),$$

so that if the asymptotic interfacial heights are the same at both far ends of the channel, equality between asymptotic imbalances of the interfacial pressure and of the mean pressure follows,

$$\langle p\rangle_{\Delta} = P_{\Delta}. \tag{18}$$

It is interesting to view the pressure imbalance from the perspective of a center of mass for the stratified fluid. For a laterally unbounded channel, the total mass of the fluid is clearly infinite, and care should be taken to avoid divergent integrals. The local center of mass horizontal coordinate for a section of the channel between $x = L_-$ and $x = L_+$ can be defined as

$$X_c^{\ell}(t) \equiv \frac{1}{M^{\ell}} \int_{L_-}^{L_+} x\big(\rho_1\eta_1(x,t) + \rho_2\eta_2(x,t)\big)\mathrm{d}x\,, \tag{19}$$

where

$$M^{\ell} \equiv \int_{L_-}^{L_+} \big(\rho_1\eta_1(x,t) + \rho_2\eta_2(x,t)\big)\mathrm{d}x \tag{20}$$

is the total mass of the fluid in the section. Differentiating with respect to time, and taking into account (11), yields

$$M^\ell \frac{dX_c^\ell}{dt} = \int_{L_-}^{L_+} (\rho_1\eta_1\overline{u}_1 + \rho_2\eta_2\overline{u}_2)\,\mathrm{d}x + \Big[(X_c^\ell - x)(\rho_1\eta_1\overline{u}_1 + \rho_2\eta_2\overline{u}_2)\Big]\Big|_{L_-}^{L^+} . \tag{21}$$

For velocities that decay sufficiently fast at infinity the end-point terms in this expression vanish and the right-hand-side is well defined in the limit $L_\pm \to \pm\infty$, being equal to the total horizontal momentum Π_1 of the fluid. Thus, the position of the center of mass for a sufficiently long section of the channel moves in the direction defined by the total horizontal momentum, as can be expected.

2.2 Small $\rho_{_\Delta}$ limit and the scaling relation between $P_{_\Delta}$ and $\rho_{_\Delta}$

Some of the results of the previous subsection can be used to unravel a particular scaling of the momentum evolution with respect to stratification. In particular, we shall focus on the class of zero-velocity initial data. As we will see later, these initial conditions also allow to derive closed-form expressions for the initial pressure imbalance.

From the equations of motion and, in particular, from the constraint $\eta_1 + \eta_2 = h$ we have

$$\partial_x\Big(\eta_1\overline{u_1u_1} + \eta_2\overline{u_2u_2} + \frac{1}{\rho_1}\eta_1\overline{p_1} + \frac{1}{\rho_2}\eta_2\overline{p_2}\Big) = \Big(\frac{1}{\rho_2} - \frac{1}{\rho_1}\Big)\eta_x P\ . \tag{22}$$

If hydrostatic equilibrium at infinity is enforced, the layer-mean pressures are given by (15), so that in the case of equal asymptotic heights, that is, $z_- = z_+ = z_0$, the interfacial pressure difference $P_{_\Delta}$ between the ends of the channel is

$$P_{_\Delta}(\rho_{_\Delta}) = P|_{-\infty}^{+\infty} = \frac{\rho_{_\Delta}}{h_1\rho_2 + h_2\rho_1}\int_{-\infty}^{+\infty}\eta_x P\,\mathrm{d}x \equiv \frac{\rho_{_\Delta}}{h_1\rho_2 + h_2\rho_1} I_P(\rho_{_\Delta})\,, \tag{23}$$

where $h_1 = h - z_0$ and $h_2 = z_0$. A couple of relevant consequences follow from this relation: First, pressure imbalances and their associated physical phenomena, such as the nonconservation of total momentum (Camassa et al. 2012) and vorticity, cannot arise in uniform density fluids. Next, and perhaps more remarkably, these phenomena cannot be detected in the Boussinesq approximation of neglecting density stratification in the inertial terms.

Relation (23) further shows that $P_{_\Delta}$ scales at least linearly with $\rho_{_\Delta}$. Of course, the integral term I_P also depends on $\rho_{_\Delta}$, so that it cannot be concluded that this linear scaling has general validity. In fact, in the limit $\rho_{_\Delta} \to 0$ with ρ_2 fixed, the scaling can be different than linear. Assume that the interfacial pressure P admits the expansion

$$\begin{aligned} &P_{_\Delta}(0) + P_{_\Delta}{}'(0)\rho_{_\Delta} + \frac{1}{2}P_{_\Delta}{}''(0)\rho_{_\Delta}^{\,2} + \dots \\ &= \frac{1}{h_1\rho_2 + h_2\rho_1} I_P(0)\rho_{_\Delta} + \frac{1}{h_1\rho_2 + h_2\rho_1} I_P'(0)\rho_{_\Delta}^{\,2} + \dots \\ &= \frac{1}{h\rho_1} I_P(0)\rho_{_\Delta} + \left[\frac{1}{h\rho_1} I_P'(0) - \frac{h_1}{h^2\rho_1^2} I_P(0)\right]\rho_{_\Delta}^{\,2} + o(\rho_{_\Delta}^{\,2}), \end{aligned} \tag{24}$$

where $o(\rho_{_\Delta}^{\,2})$ denotes, as usual, terms going to zero faster than $\rho_{_\Delta}^{\,2}$. This implies that $I_P(\rho_{_\Delta}) \to 0$ as $\rho_{_\Delta} \to 0$ for localized displacements of the interface. Equating term by term yields $P_{_\Delta}(0) = 0$, as already manifest from (23). Now, for a homogeneous fluid, equation (16) shows that horizontal momentum is conserved if $P_{_\Delta}(0) = 0$. On the other hand, recalling that the time variation of each layer's total horizontal momentum is

$$\frac{d\Pi_{1j}}{dt} \equiv \frac{d}{dt}\int_{-\infty}^{+\infty}\rho_j\eta_j\overline{u}_j\,\mathrm{d}x + \rho_j\eta_j\overline{u_ju_j}|_{-\infty}^{+\infty} = -\,\eta_j\overline{p_j}|_{-\infty}^{+\infty} + (-1)^j I_P, \quad j = 1, 2\,, \tag{25}$$

we can see that if the upper and lower layer momentum are separately conserved, then not only $P_{\Delta} = 0$, but also $I_P = 0$. Indeed, the lateral equilibrium boundary conditions imply that for each infinite upper and lower layer the horizontal momenta are conserved if and only if

$$-h_1 P_{\Delta} - I_P = 0\,, \qquad -h_2 P_{\Delta} + I_P = 0\,, \tag{26}$$

at all times, that is, if and only if

$$I_P = 0 \qquad \text{and} \qquad P_{\Delta} = 0\,. \tag{27}$$

Now, given that $\rho_{\Delta} = 0$ implies horizontal momentum conservation, and for zero initial velocities the initial value of each layer's total horizontal momentum is clearly zero, the conserved value of the horizontal momentum in each layer is null for all times (and hence so is the total fluid's horizontal momentum). Therefore (27) shows that the linear term in expansion (24) vanishes. Thus, for zero velocities, $P_{\Delta}(\rho_{\Delta})$ is at least quadratic in ρ_{Δ}, since from (24) we obtain

$$P_{\Delta} = \frac{1}{h_1\rho_2 + h_2\rho_1} I_P'(0)\rho_{\Delta}^{\,2} + o(\rho_{\Delta}^{\,2}). \tag{28}$$

Notice that this result is general for zero-velocity initial conditions. If the velocity of the system is different from zero, the difference of pressure between the ends of the channel can be expected, in general, to scale linearly with the density difference ρ_{Δ}, at least initially in time.

We remark that, if different asymptotic heights are enforced on the fluid's configuration, formula (23) has to be modified as

$$\frac{\rho_{\Delta}}{\rho_1\rho_2} I_P(\rho_{\Delta}) = \left(\frac{h - z_+}{\rho_1} + \frac{z_+}{\rho_2}\right) P(+\infty) - \left(\frac{h - z_-}{\rho_1} + \frac{z_-}{\rho_2}\right) P(-\infty) + gh(z_+ - z_-)\,. \tag{29}$$

We will henceforth refer to this case as the "kink-like" configuration. Its limiting case, by which one or both of the two different asymptotic heights reach the channel's boundaries, will be referred to as "dam-like."

2.3 Interfacial pressure imbalance and total vorticity

Next, we briefly examine how the asymptotic interface pressure differential P_{Δ} is related with variation of the total vorticity. This link can be obtained from the Helmoltz-type equation for the vorticity,

$$\boldsymbol{\omega}_t + \nabla \times (\boldsymbol{\omega} \times \mathbf{v}) = -\nabla\left(\frac{1}{\rho}\right) \times \nabla p. \tag{30}$$

For a system in the strip $\mathcal{S} = \mathbb{R} \times [0, h]$, the total vorticity is

$$\boldsymbol{\Gamma} = \int_{\mathbb{R}\times[0,h]} \boldsymbol{\omega}\, \mathrm{d}A\,. \tag{31}$$

Its time variation follows directly by integrating (30), and by using the Green-Stokes' formula. Taking into account the boundary conditions on the velocity field yields

$$\frac{d\,\boldsymbol{\Gamma}}{dt} = \int_{\mathbb{R}\times[0,h]} \nabla p \times \nabla\left(\frac{1}{\rho}\right)\, \mathrm{d}A\,. \tag{32}$$

Notice that any barotropic component of the pressure $p_b = p_b(\rho)$ will not contribute to this formula, which ultimately rephrases the content of the Bjerknes theorem (see, e.g., Yih (1980)) applied to the whole fluid domain.

We now consider the two-layer case. In this case, $\rho = \rho_2 - H(z - \eta(x,t))\rho_{\Delta}$ (by denoting the Heaviside function as H), and hence the gradient of $1/\rho$ is

$$\nabla\left(\frac{1}{\rho}\right) = \begin{pmatrix} -\eta_x \\ 1 \end{pmatrix} \frac{\rho_{\Delta}}{\rho_1\rho_2} \delta(z - \eta(x,t)), \tag{33}$$

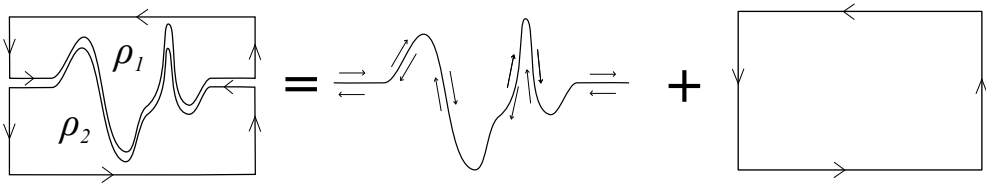

Figure 2: The contours for Stokes theorem in the case of a two-layer fluid.

which is normal to the interface $\eta(x,t)$. The integrand in the total vorticity derivative (32) will then involve products of ∇p-components with a delta-function. Such products are well defined, in general, only if the functions multiplying the Dirac-δ are continuous. In our case, while the component of the pressure gradient normal to the interface suffers a jump, the tangential component is continuous, and hence so is the δ multiplier. We have

$$\nabla p \times \nabla \left(\frac{1}{\rho}\right) = -(p_x + p_z\eta_x)\frac{\rho_\Delta}{\rho_1\rho_2}\delta(z-\eta(x,t))\,\mathbf{j}, \tag{34}$$

where $\mathbf{j}$ is the unit vector normal to the fluid plane. Similar care is needed to apply the Green-Stokes formula in the two-layer case, because the integrand is again singular at the interface, in general. The contour of integration has to be modified by separating the different domains where the density is constant, thereby breaking the contour path used in the smooth density case into two paths enclosing the domain of each fluid. This decomposition, depicted in figure 2, reduces the problem to evaluating the contour integration at the interface, because the contributions of the channel boundaries vanish for the same reason as for the smooth density case. In this paper we will be concerned mainly with the case of zero-velocity initial conditions, so that the fluid vorticity $\boldsymbol{\omega}$ is concentrated on the interface γ in a vortex sheet (see also Yih, 1980, p. 14). Therefore the kinetic contribution to $\mathrm{d}\Gamma/\mathrm{d}t$ is

$$\int_\gamma (\boldsymbol{\omega}\times\boldsymbol{v_1})\cdot\mathbf{dr} - \int_\gamma (\boldsymbol{\omega}\times\boldsymbol{v_2})\cdot\mathbf{dr} = \int_\gamma \boldsymbol{\omega}\times(\boldsymbol{v_2}-\boldsymbol{v_1})\cdot\mathbf{dr}. \tag{35}$$

Since the shear velocity $\boldsymbol{v_2}-\boldsymbol{v_1}$ is tangent to the interface, these line integrals also vanish and, with zero-velocity initial conditions, formula (32) still holds. Thus, by using (34) we can express the time variation of the total vorticity in terms of the (interface) pressure imbalance as

$$\begin{aligned}\frac{d\Gamma}{dt} &= \int_{-\infty}^{\infty}\left(\int_0^h (p_x+p_z\eta_x)\frac{\rho_\Delta}{\rho_1\rho_2}\delta(z-\eta(x,t))\,\mathrm{d}z\right)\mathrm{d}x\\ &= \frac{\rho_\Delta}{\rho_1\rho_2}\int_{-\infty}^{\infty}(p_x+p_z\eta_x)|_{z=\eta(x,t)}\,\mathrm{d}x = \frac{\rho_\Delta}{\rho_1\rho_2}\int_{-\infty}^{\infty}\frac{dP}{dx}\,\mathrm{d}x\\ &= \frac{\rho_\Delta}{\rho_1\rho_2}\big(P(+\infty)-P(-\infty)\big) = \frac{\rho_\Delta P_\Delta}{\rho_1\rho_2},\end{aligned} \tag{36}$$

where we have used the definition $P(x)=p(x,\eta(x))$.

Formula (36), connecting the time variation of the total vorticity with the asymptotic pressure imbalance, has to be corrected if the interface touches the boundary of the channel. Indeed, let $\mathcal{C}$ be the set in which the interface coincides with one of the boundaries (see figure 3). For $x\in\mathcal{C}$ and every $z\in[0,h]$ the gradient of the density is zero, so that the set $\mathcal{C}\times[0,h]$ does not contribute to the total vorticity time-variation. Therefore

$$\frac{d\Gamma}{dt} = \frac{\rho_\Delta}{\rho_1\rho_2}\int_{\mathbb{R}/\mathcal{C}}\frac{dP}{dx}\,\mathrm{d}x = \frac{\rho_\Delta}{\rho_1\rho_2}\Big(P_\Delta - \sum_{i=1}^{n}\left[p\left(x_i^R,\eta\left(x_i^R\right)\right)-p\left(x_i^L,\eta\left(x_i^L\right)\right)\right]\Big). \tag{37}$$

We remark that the correction terms might be, in some cases, dominant. Indeed, for vanishing velocity initial configurations, P_Δ behaves as ρ_Δ^2, while the point contributions can produce linear terms in ρ_Δ.

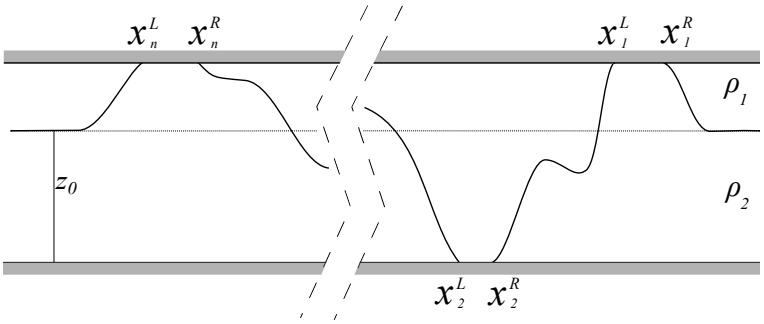

Figure 3: Sketch of a typical interface configuration for a two-fluid density distribution for which boundary contributions are relevant.

3 Long-wave models

We now briefly describe strongly nonlinear long-wave models for two-layer fluids (see, e.g., Choi & Camassa, 1999). Variants of these models have been extensively studied in the literature, especially for the classical dispersionless limit, see for instance Baines's (1995) monograph, and, more recently, Milewski et al. (2004) and Boonkasame & Milewski (2012) for a study of the stability properties of the motion governed by these models. While derived under the long-wave approximation, the dispersive case has been studied in the context of an internal "dam-breaking" problem (which leads to high wavenumber initial conditions) by Esler & Pearce (2011) in the Boussinesq regime; we will return to this class of initial conditions for the parent Euler system in §5. By using these models, one can derive in a relatively straightforward manner fairly general results, whose fidelity with respect to the parent Euler equations can be tested on explicit solutions for special configurations (typically for zero-velocity initial data). Thus, in this section we anticipate some of the results that will be computed explicitly later on for the special configurations of vanishing initial velocity within the *full* Euler equation study. We remark that models may differ substantially in their effectiveness to predict the "true" physical behaviour of the systems under consideration. For instance, as mentioned in Section 2, the Boussinesq limit (of both models) does not capture any pressure imbalance; in turn, the dispersionless limit notably yields a vanishing pressure imbalance for the vanishing velocity case. As already highlighted in Camassa et al. (2012), a non-vanishing pressure imbalance in the static case can be obtained by taking into account dispersive terms in the strongly nonlinear models.

3.1 Equations of motion

For a two-layer incompressible Euler fluid in a channel of height h, the equations of motion (11)–(12) can be written as

$$\overline{u_i}_t + \overline{u_i}\,\overline{u_i}_x + (-1)^i g\eta_{ix} = -\frac{P_x}{\rho_i} + D_i(u_i, v_i, \eta_i), \quad \eta_{it} + (\eta_i\overline{u_i})_x = 0, \qquad i = 1, 2, \tag{38}$$

where $\eta_1 + \eta_2 = h$, and the terms denoted by D_i lump all the contributions from pressure, vertical velocity components and from switching layer-averages with products. Shallow water long-wave models can be derived from this in the case when the layer thicknesses are small with respect to a typical wavelenght L, by retaining only the leading order terms in D_i, and provide effective approximations of (two-layer) incompressible Euler fluid (see. e.g., Choi & Camassa, 1999). Denoting the small parameter of the model by $\delta \equiv h/L$, at the first order in δ the hydrostatic equilibrium is valid everywhere and the relations (15) hold not only asymptotically but along the whole channel. Also, at this order $D_i = 0$, i.e., system (38) is turned into its dispersionless limit

$$\overline{u_i}_t + \overline{u_i}\,\overline{u_i}_x + (-1)^i g\eta_{ix} = -\frac{P_x}{\rho_i}, \qquad \eta_{it} + (\eta_i\overline{u_i})_x = 0, \qquad i = 1, 2. \tag{39}$$

In case of zero asymptotic velocities the total flux $Q(t) \equiv \eta_1 \overline{u_1} + \eta_2 \overline{u_2}$ is zero. Solving for P_x the dispersionless equations (39) and using the constraint $\eta_1 + \eta_2 = h$, yields for the interface pressure asymptotic difference the (dispersionless) formula

$$P_{\Delta} = h \int_{-\infty}^{\infty} \frac{(\overline{u_1}\ \overline{u_2})_x}{\eta_1/\rho_1 + \eta_2/\rho_2}\, \mathrm{d}x\,, \tag{40}$$

which is equivalent to the form of P_{Δ} reported in Camassa et al. (2012). We remark that in the Boussinesq approximation the integrand becomes a total derivative, and hence this pressure difference P_{Δ} is zero (see, e.g., Milewski et al. 2004) for localized velocities. This fact should not be regarded as a surprise, since pressure imbalances are phenomena due to the relative inertia of the stratified fluid, and not to the relative buoyancy. The integrand in (40) is also a total spatial derivative, and hence $P_{\Delta} = 0$, when the interface is flat, independently of the Boussinesq approximation. In fact, the same conclusion holds for the full Euler system, as seen from (23), since for a flat interface $\eta_x = 0$. However, the dispersionless formula (40) goes too far, as it also predicts $P_{\Delta} = 0$ whenever the layer-mean velocities vanish. By restoring the dispersive terms in the strongly nonlinear model, we show next that this conclusion might not be warranted in general.

3.2 Effects of dispersion

The vanishing of the leading order term (40) for zero-velocities requires that the dispersive terms D_i of equation (38) be estimated within the same long-wave asymptotic approach. If such terms are retained, relation (40) reads

$$P_{\Delta} = \int_{-\infty}^{+\infty} \left(\frac{\eta_1}{\rho_1} + \frac{\eta_2}{\rho_2}\right)^{-1} \left[h\,(\overline{u}_1 \overline{u}_2)_x + (\eta_1 D_1 + \eta_2 D_2)\right]\, \mathrm{d}x\,. \tag{41}$$

The first nontrivial dispersion contribution is given asymptotically as $\delta \to 0$ by (see Choi & Camassa, 1999)

$$D_i \sim \frac{1}{3\eta_i} \left(\eta_i^3 \left(\overline{u_i}_{xt} + \overline{u_i}\ \overline{u_i}_{xx} - (\overline{u_i}_x)^2\right)\right)_x\,, \qquad i = 1, 2. \tag{42}$$

If $\overline{u}_i = 0$, this implies

$$P_{\Delta} \sim \frac{1}{3} \int_{-\infty}^{\infty} \left(\frac{\eta_1}{\rho_1} + \frac{\eta_2}{\rho_2}\right)^{-1} \left(\eta_1^3\, \overline{u}_{1tx} + \eta_2^3\, \overline{u}_{2tx}\right)_x\, \mathrm{d}x\,. \tag{43}$$

A consistent approximation of this formula can be given by inserting the expressions for the $\overline{u}_{it}$'s obtained in the zero-dispersion limit. The dispersionless equation of motions (39), when the velocities are near zero, yield

$$\overline{u_1}_t \sim \rho_{\Delta} g \frac{\eta_2 \eta_{2x}}{\rho_1 \eta_2 + \rho_2 \eta_1}, \qquad \overline{u_2}_t \sim -\frac{\eta_1}{\eta_2} \overline{u_1}_t = \rho_{\Delta} g \frac{\eta_1 \eta_{1x}}{\rho_1 \eta_2 + \rho_2 \eta_1} \tag{44}$$

asymptotically as $\delta \to 0$. Therefore

$$P_{\Delta} \sim \frac{\rho_{\Delta} g}{3} \int_{-\infty}^{\infty} \left(\frac{\eta_1}{\rho_1} + \frac{\eta_2}{\rho_2}\right)^{-1} \left(\eta_1^3 \left(\frac{\eta_2 \eta_{2x}}{\rho_1 \eta_2 + \rho_2 \eta_1}\right)_x + \eta_2^3 \left(\frac{\eta_1 \eta_{1x}}{\rho_1 \eta_2 + \rho_2 \eta_1}\right)_x\right)_x\, \mathrm{d}x. \tag{45}$$

When ρ_{Δ} is small, this asymptotic relation can be simplified to

$$P_{\Delta} \sim \frac{\rho_{\Delta} g}{3h} \int_{-\infty}^{\infty} \left(\frac{1}{h} + \frac{\eta_2}{h^2} \frac{\rho_{\Delta}}{\rho_1}\right) \left(\eta_1^3\, (\eta_2 \eta_{2x})_x + \eta_2^3\, (\eta_1 \eta_{1x})_x\right)_x\, \mathrm{d}x + o(\rho_{\Delta}^2).$$

The linear term in ρ_{Δ} is a total derivative in x and therefore does not contribute to P_{Δ}, confirming the general results of the previous section. As expected, the first nonzero term for P_{Δ} is proportional to ρ_{Δ}^2,

$$P_{\Delta} \sim \frac{\rho_{\Delta}^2 g}{6\rho_1 h^3} \int_{-\infty}^{\infty} \eta_2 \left(\eta_1^3 \left(\eta_2^2\right)_{xx} + \eta_2^3 \left(\eta_1^2\right)_{xx}\right)_x\, \mathrm{d}x + o(\rho_{\Delta}^2). \tag{46}$$

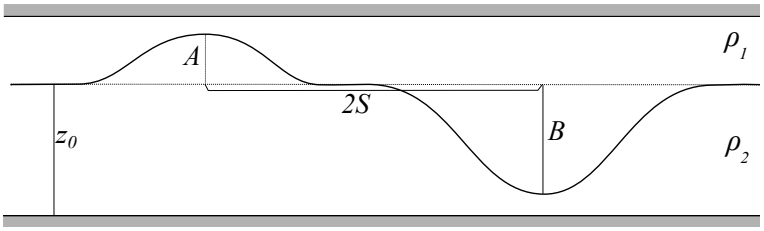

Figure 4: A two-bump configuration. Only when S is comparable with the typical width of the bumps the pressure difference P_Δ is significantly different from zero.

This estimate allows explicit analytic computations of P_Δ for special cases. For instance, when the interface profile is

$$\eta(x) = z_0 + A\exp\left(-(x+S)^2/\sigma^2\right) - B\exp\left(-(x-S)^2/\sigma^2\right), \tag{47}$$

(see figure 4) the asymptotic pressure difference is given by

$$P_\Delta \sim \frac{64\sqrt{3\pi}g}{81\rho_1}\frac{S^3 e^{-\frac{8S^2}{3\sigma^2}}}{\sigma^5}AB(A+B)\rho_\Delta^2 + o(\rho_\Delta^2). \tag{48}$$

Here, for long-wave asymptotic consistency, σ should be taken sufficiently large; also the parameters A and B need to be such that the extrema of function (47) do not touch the channel boundary.

Some interesting conclusions can be extracted from (48). First, if $A = -B$ the interface of the system becomes symmetric and, as always in these configurations, $P_\Delta = 0$ (see Camassa et al. 2012). Second, explicit dependence on the asymptotic height z_0 does not appear in formula (48). However, notice that the ranges of A and B are constrained by the choice of z_0 if the interface has to stay away from boundaries. Thus, by choosing, e.g., $A + B = k$ and $B = z_0 - s$ (for given parameters k and s) we fix the maximum and the minimum of the interface leaving only z_0 as a free variable. In this case P_Δ is a quadratic function of the interface height z_0 and the extremum of this quadratic relation is at $A = B$. Third, the most interesting behaviour is related to the dependence on the separation parameter S. If the two bumps are well separated ($S \gg \sigma$), then P_Δ is exponentially small. However, when the supports of the two bumps have an intersection ($S \simeq \sigma$), then P_Δ is nonzero to leading order $O(\rho_\Delta^2)$.

4 Full Euler system: pressure jump at t = 0 in the small ρ_Δ asymptotic limit

We consider again the full Euler system for a two-layer fluid with zero initial velocity. As seen in Section 2.2, in this case the expansion in ρ_Δ of the pressure imbalance starts with the quadratic term. We now compute this term explicitly. Throughout this section, unless otherwise stated, we will reference density to that of the lower fluid, so that $\rho_2 = 1$.

4.1 The small ρ_Δ expansion

Consider an initial condition for the two-fluid stratification such as the one depicted in figure 1. Let the initial velocity be identically zero, with the fluid in hydrostatic equilibrium as $|x| \to \infty$. In this case, the Euler equations (1) determine the pressure $p(x, z)$ at time $t = 0$ through the solution of the elliptic equation

$$\nabla \cdot \left(\frac{1}{\rho}\nabla p\right) = 0\,, \tag{49}$$

subject to the Neumann boundary conditions

$$\frac{\partial p}{\partial x} \to 0 \quad \text{as} \quad |x| \to \infty\,, \qquad \frac{\partial p}{\partial z} = -g\rho \quad \text{at} \quad z = 0, h\,. \tag{50}$$

Of course, non-differentiability of the density distribution for the case of figure 1 requires an appropriate interpretation of equation (49). We will enforce (49) separately in each of the ρ_1 and ρ_2 domains, Ω_1 and Ω_2 say,

$$\nabla^2 p = 0\,, \qquad (x,z) \in \Omega_i, \quad i = 1,2\,,$$

so that p is harmonic in each subdomain, and assign boundary conditions at the discontinuities of ρ. These consist of continuity of p everywhere, while its normal derivatives jump according to the "flux-continuity" condition

$$\frac{1}{\rho_1}\frac{\partial p}{\partial n}\bigg|_1 = \frac{1}{\rho_2}\frac{\partial p}{\partial n}\bigg|_2\,, \tag{51}$$

with obvious meaning of the notation.

Let the variable density be defined as a perturbation away from a uniform density fluid

$$\rho = \rho_2 - \epsilon r(x,z)\,, \qquad 0 < \epsilon \ll 1, \tag{52}$$

where r positive, so that ρ_2 is the maximum density of fluid. For notational convenience, we further choose units in such a way that $h = 1$, and $g = 1$. We seek a solution for the pressure equation as an asymptotic expansion

$$p = p^{(0)} + \epsilon p^{(1)} + \epsilon^2 p^{(2)} + o(\epsilon^2) \tag{53}$$

whence, equating like-powers of ϵ,

$$\nabla^2 p^{(0)} = 0\,, \quad \nabla^2 p^{(1)} + \nabla\cdot(r\,\nabla p^{(0)}) = 0\,, \quad \nabla^2 p^{(2)} + \nabla\cdot(r\,\nabla p^{(1)}) + \nabla\cdot(r^2\nabla p^{(0)}) = 0\,,\ldots \tag{54}$$

with boundary conditions, respectively,

$$\begin{aligned} &\frac{\partial p^{(0)}}{\partial z}\bigg|_{z=0,1} = -1\,, \qquad \frac{\partial p^{(1)}}{\partial z}\bigg|_{z=0,1} = r|_{z=0,1}\,, \qquad \frac{\partial p^{(2)}}{\partial z}\bigg|_{z=0,1} = 0\,, \\ &\frac{\partial p^{(k)}}{\partial x} \to 0 \quad \text{as} \quad |x| \to \infty \ \text{ for } k \geq 0. \end{aligned} \tag{55}$$

The $O(\epsilon^0)$-equation is simply solved by $p^{(0)} = -z + \text{const.}$, which yields the equation for $p^{(1)}$ in the form

$$\nabla^2 p^{(1)} = r_z\,.$$

Since the fluid is two-layer, still denoting the usual Heaviside function as H, we have

$$r(x,z) = H(z - \eta(x)),$$

where the interface location $z = \eta(x)$ behaves as

$$\eta(x) \to z_\pm \quad \text{as} \quad x \to \pm\infty\,, \qquad 0 < \eta(x) < 1\,.$$

This means that the heavy fluid density is $\rho_2 = 1$ and the light fluid density is $\rho_1 = 1-\epsilon$, so that, in the chosen units, $\rho_\Delta = \epsilon$. Let

$$p^{(1)} = p_h^{(1)} + (z - z_0)H(z - z_0)\,, \tag{56}$$

where z_0 is any reference height. The summand $(z-z_0)H(z-z_0)$ takes care of the top and bottom boundary conditions, leaving a homogeneous Neumann problem for $p_h^{(1)}(x,z)$ in the infinite strip. The equation for $p_h^{(1)}(x,z)$ is then

$$\nabla^2 p_h^{(1)} = \delta(z-\eta(x)) - \delta(z-z_0)\,. \tag{57}$$

To solve this we can make use of the identity

$$\sum_{n=1}^{\infty}\cos(n\pi\theta) = -\frac{1}{2} + \delta_p(\theta) \equiv -\frac{1}{2} + \sum_{k=-\infty}^{+\infty}\delta(\theta+2k)\,,$$

from the theory of distributions (Gelfand & Shilov, 1964). Indeed, we have

$$\begin{aligned} 2\sum_{n=1}^{\infty}\cos(n\pi z)\cos(n\pi\eta) &= \sum_{n=1}^{\infty}\Big(\cos\big(n\pi(z-\eta)\big) + \cos\big(n\pi(z+\eta)\big)\Big) \\ &= -1 + \delta_p(z-\eta) + \delta_p(z+\eta) = -1 + \delta(z-\eta) \end{aligned}$$

since $0<z<1$ and $0<\eta<1$, so that the support of the second Dirac-δ always falls outside the channel. For the same reason the periodic shifts can be ignored for the first δ. Hence, we are lead to the following expression of the right-hand side of (57):

$$\delta(z-\eta(x)) - \delta(z-z_0) = 2\sum_{n=1}^{\infty}\cos(n\pi z)(\cos(n\pi\eta(x)) - \cos(n\pi z_0)), \tag{58}$$

from which, taking the homogeneous Neumann boundary conditions into account, the coefficient of the Fourier series expression of $p_h^{(1)}(x,z)$ can be read off. Indeed,

$$p_h^{(1)}(x,z) = \sum_{n=0}^{\infty} a_n(x)\cos(n\pi z) \tag{59}$$

yields

$$a_n'' - n^2\pi^2 a_n = 2(\cos(n\pi\eta(x)) - \cos(n\pi z_0)) \text{ for } n \geq 0.$$

For $n=0$, $a_0''=0 \Leftrightarrow a_0 = $ constant, say $a_0=0$. For $n>0$, the equation for a_n can be solved by use of the Green function for the operator $\partial_x^2 - n^2\pi^2$ on the real line,

$$G_n(x,\xi) = -\frac{1}{2n\pi}e^{-n\pi|x-\xi|}\,,$$

to finally obtain

$$p_h^{(1)}(x,z) = \int_{-\infty}^{+\infty}\sum_{n=1}^{\infty}\frac{e^{-n\pi|x-\xi|}}{n\pi}\cos(n\pi z)\Big(\cos(n\pi z_0) - \cos(n\pi\eta(\xi))\Big)\,\mathrm{d}\xi\,. \tag{60}$$

This expression shows that the layer-average of $p_h^{(1)}$ is always zero at any fixed x-location, as integration of $\cos(n\pi z)$ vanishes for all n. Since the average of $p^{(0)}$ and the component $(z-z_0)H(z-z_0)$ of (56) is the same for any fixed x, we can conclude that no contribution to the average pressure differential $\langle p(+\infty)\rangle - \langle p(-\infty)\rangle$ can arise at order ϵ, as expected from the results of Section 2.2, and the fact that, for equal asymptotic interfacial heights, the average and interface pressure imbalances are equal.

Next, we work on the second order pressure contribution $p^{(2)}$. We concentrate only on the layer-average of the boundary term $\partial_x p^{(2)}$ instead of the exact z-dependence. Multiplying the $p^{(2)}$ equation by x, integrating over the fluid volume and taking into account the boundary conditions yields

$$\lim_{L\to\infty}\int_0^1 \big(p^{(2)}(L,z) - p^{(2)}(-L,z)\big)\,\mathrm{d}z = -\lim_{L\to\infty}\int_{[-L,+L]\times[0,1]} r\,\partial_x p^{(1)}\,\mathrm{d}x\,\mathrm{d}z.$$

The top and bottom boundary contributions cancel out exactly from the $p_h^{(1)}$ and $p^{(2)}$ terms. Passing to the limit we retrieve a close relative of the general formula for the pressure differential in an infinite strip,

$$\langle p^{(2)} \rangle_\Delta \equiv \int_0^1 \big(p^{(2)}(\infty, z) - p^{(2)}(-\infty, z) \big) \, \mathrm{d}z = - \int_{\mathbb{R}\times[0,1]} r \, \partial_x p^{(1)} \, \mathrm{d}x \, \mathrm{d}z. \tag{61}$$

Substituting expression (60) for $p_h^{(1)}$ yields

$$\begin{aligned} \langle p^{(2)} \rangle_\Delta = - \int_{-\infty}^{+\infty} \Bigg(\int_{-\infty}^{+\infty} \mathrm{sgn}(x-\xi) \sum_{n=1}^{\infty} e^{-n\pi|x-\xi|} \left(\cos(n\pi\eta(\xi)) - \cos(n\pi z_0) \right) \mathrm{d}\xi \, \times \\ \times \int_0^1 \cos(n\pi z) H(z - \eta(x)) \, \mathrm{d}z \Bigg) \, \mathrm{d}x \, . \end{aligned} \tag{62}$$

The last integral is

$$\int_{\eta(x)}^1 \cos(n\pi z) \, \mathrm{d}z = -\frac{1}{n\pi} \sin(n\pi\eta(x))$$

and hence

$$\begin{aligned} \langle p^{(2)} \rangle_\Delta = \sum_{n=1}^{\infty} \int_{-\infty}^{+\infty} \sin(n\pi\eta(x)) \times \\ \times \left(\int_{-\infty}^{+\infty} \mathrm{sgn}(x-\xi) \, \frac{e^{-n\pi|x-\xi|}}{n\pi} \big(\cos(n\pi\eta(\xi)) - \cos(n\pi z_0) \big) \, \mathrm{d}\xi \right) \mathrm{d}x. \end{aligned} \tag{63}$$

We remark that all the theoretical arguments for the determination of the pressure jump $\langle p^{(2)} \rangle_\Delta$ have assumed that the interface does not touch the channel boundary. Thus, we assume that there are always slivers of light and heavy fluid near the top and bottom lid, respectively. However, it is not difficult to realize that, since all integrals are bounded, and the integrands decay exponentially, we can pass to the limit of zero sliver-width in the above formulae. Furthermore, since $p^{(2)}$ is no longer affected by the density difference at the top and bottom interfaces, this limit coincides with the "physical" instance of zero sliver-width. Indeed, the density difference is taken care by $p^{(1)}$, while $p^{(2)}$ satisfies a Neumann problem with vanishing boundary conditions at $z = 0$ and $z = 1$. It is however suitable to anticipate here that, in general, care should be taken in performing such limits for general density values. In particular, in Appendix C we shall show that the behaviour of $p(x, z)$ in "air-water" systems, obtained by considering the limit $\rho_1 \to 0$, might not follow from the *naïve* limit of vanishing sliver width.

4.2 Comparison with the long wave model

Expression (63) can be used to test the long-wave model result (46) with, e.g., $\eta(x)$ given by (47). While we are unable to compute the integrals in (63) explicitly, their numerical evaluation for up to 25 terms in the series yields agreement over a broad range of parameters. Table 1 reports a few examples. For these, the long wave model pressure imbalance (46) is always of the same order of its Euler counterpart (63), with the discrepancy decreasing as the main long wave parameter σ increases. Remarkably, the agreement is acceptable already for $\sigma = 3\sqrt{8/3} \simeq 4.9$, which for a channel of height $h = 1$ would correspond to a value of the long-wave small parameter $\delta \simeq 0.2$. The trend exemplified by table 1 persists in general for all the parameter combinations we have checked.

We note that the convergence of the series in (63) is slow for the class of smooth profiles from (47) we have explored, which partially adds to the discrepancy in table 1. In fact, a general convergence proof and an estimate of the convergence rate shows that the series coefficients are bounded by $1/n^2$, for any interface function η of bounded variation class. Next, we focus instead on special profiles where the series summation can be performed explicitly.

Table 1: Comparison of pressure imbalances P_Δ/ρ_Δ^2 as predicted by long-wave model and full Euler results for interface (47) with asymptotic height $z_0 = 1/2$.

A	B	σ	S	Model (eqn. (48))	Euler (eqn. (63))	Model/Euler
1/3	1/3	$\sqrt{8/3}$	1	5.69×10^{-3}	4.01×10^{-3}	1.42
2/5	1/5	$\sqrt{8/3}$	1	3.69×10^{-3}	2.62×10^{-3}	1.40
3/5	1/3	$2\sqrt{8/3}$	1	9.49×10^{-4}	8.25×10^{-4}	1.15
3/5	1/3	$3\sqrt{8/3}$	1	1.44×10^{-4}	1.32×10^{-4}	1.09
4/5	1	$4\sqrt{8/3}$	1	2.76×10^{-4}	2.57×10^{-4}	1.07
3/5	2/3	$4\sqrt{8/3}$	3	1.59×10^{-3}	1.49×10^{-3}	1.06
1/3	1/3	$4\sqrt{8/3}$	20	1.68×10^{-12}	1.70×10^{-12}	0.99

4.3 Special initial conditions: piecewise-constant interfaces

Let us consider the integral formula (63) for a profile η that is smooth on the whole line, except possibly at a finite number of points $A_1, A_2, \ldots, A_N$, where the jumps $\eta(A_\alpha^+) - \eta(A_\alpha^-)$ are finite. We also require, as usual, that $\lim_{x\to\pm\infty} \eta(x) = z_\pm$ for some asymptotic values $z_\pm$. Taking into account the distributional identity

$$\operatorname{sgn}(x-\xi)e^{-n\pi|x-\xi|} = \frac{1}{n\pi}\frac{d}{d\xi}e^{-n\pi|x-\xi|},$$

integrating by parts, and considering the distributional derivative of $\cos(n\pi\eta(\xi))$, leads to an expression equivalent to (63),

$$\begin{aligned}\langle p^{(2)}\rangle_\Delta = &\sum_{n=1}^{\infty}\frac{1}{n\pi}\int_{-\infty}^{+\infty}\sin(n\pi\eta(x))\left(\int_{-\infty}^{+\infty}e^{-n\pi|x-\xi|}\eta'(\xi)\sin(n\pi\eta(\xi))\,\mathrm{d}\xi\right)\mathrm{d}x\\ -&\sum_{n=1}^{\infty}\frac{1}{n^2\pi^2}\sum_{\alpha=1}^{N}\int_{-\infty}^{+\infty}\mathrm{d}x\sin(n\pi\eta(x))e^{-n\pi|x-A_\alpha|}\left(\cos(n\pi\eta(A_\alpha^-))-\cos(n\pi\eta(A_\alpha^+))\right)\mathrm{d}x.\end{aligned} \tag{64}$$

Now, for piecewise-constant interface profiles

$$\begin{aligned}&\eta(\xi) = z_i \quad \text{for } A_i < \xi < A_{i+1},\ i = 1,\ldots,N-1,\\ &\eta(\xi) = z_- \equiv z_0 \text{ for } \xi < A_1 \text{ and } \eta(\xi) = z_+ \equiv z_N \text{ for } \xi > A_N,\end{aligned} \tag{65}$$

only the second line of equation (64) provides a contribution, and we have $\eta(A_\alpha^-) = z_{\alpha-1}$, $\eta(A_\alpha^+) = z_\alpha$.

Because of the shape achieved by each fluid's domain in the limiting three step case with $z_1 = 0$ and $z_2 = 1$, i.e., disconnected domains with no connecting slivers at the top and bottom plates, in what follows we will often refer to this class of initial conditions as "hooks," see figure 5. We remark that these are possibly the simplest configurations yielding explicit expressions for non-vanishing pressure imbalances. Moreover, hooks can in principle be implemented experimentally by use of gates separating the fluids, just as in the limiting configuration of the dam-break case (corresponding to $z_0 = 0$, $z_3 = 1$, $z_1 = z_2 = 0$, all A's zero) with a single gate spanning the whole width of the channel.

Performing the integrations in (64) we get that the pressure jump at the second order in the ρ_Δ expansion is given by

$$\langle p^{(2)}\rangle_\Delta = \sum_{k=1}^{\infty}\frac{1}{\pi^3\,k^3}\left(\Delta_0^{(k)} + \sum_{1\le\alpha<\beta\le N}\Delta_{[\alpha,\beta]}^{(k)}\mathrm{e}^{k\pi(A_\alpha - A_\beta)}\right), \tag{66}$$

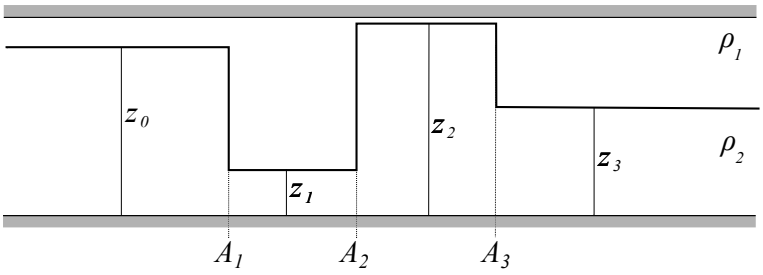

Figure 5: Initial hook-like configuration for a two-fluid density distribution in an x-infinite channel between two rigid plates located at $z = 0, 1$.

where

$$\Delta_0^{(k)} = \sum_{\alpha=1}^{N} \sin(k\pi(z_\alpha - z_{\alpha-1})) + \frac{1}{2}\left(\sin(2k\pi\, z_0) - \sin(2k\pi\, z_N)\right), \tag{67}$$

and

$$\begin{aligned}\Delta_{[\alpha,\beta]}^{(k)} = &(\cos(k\pi\, z_\beta) - \cos(k\pi\, z_{\beta-1}))(\sin(k\pi\, z_\alpha) - \sin(k\pi\, z_{\alpha-1}) + \\ &- (\cos(k\pi\, z_\alpha) - \cos(k\pi\, z_{\alpha-1}))(\sin(k\pi\, z_\beta) - \sin(k\pi\, z_{\beta-1})),\end{aligned} \tag{68}$$

or, equivalently,

$$\begin{aligned}\Delta_{[\alpha,\beta]}^{(k)} = &\sin(k\pi(z_\alpha - z_\beta)) - \sin(k\pi(z_{\alpha-1} - z_\beta)) + \\ &- \sin(k\pi(z_\alpha - z_{\beta-1})) + \sin(k\pi(z_{\alpha-1} - z_{\beta-1})).\end{aligned} \tag{69}$$

In particular, for the 'three-jump' case, with discontinuities located at $A_1 \le A_2 \le A_3$ and arbitrary heights $0 \le z_0, z_1, z_2 \le 1$, $z_0 = z_3$, we have

$$\begin{aligned}\langle p^{(2)}\rangle_\Delta = &\sum_{k=1}^{\infty} \frac{1}{\pi^3\, k^3}\Big[\left(\sin(k\pi(z_1 - z_0)) + \sin(k\pi(z_2 - z_1)) + \sin(k\pi(z_0 - z_2))\right) \\ &\times \left(1 - \mathrm{e}^{k\pi(A_1 - A_2)}\right)\left(1 - \mathrm{e}^{k\pi(A_2 - A_3)}\right)\Big].\end{aligned} \tag{70}$$

Setting for simplicity $A_3 = -A_1 = A$, $A_2 = 0$, and $z_1 = 0$, $z_2 = 1$, yields the compact expression

$$\langle p^{(2)}\rangle_\Delta = -2\sum_{n=0}^{\infty} \frac{\sin((2n+1)\pi z_0)}{((2n+1)\pi)^3}\left(1 - e^{-(2n+1)\pi A}\right)^2. \tag{71}$$

If A is sufficiently large the exponentials can be neglected and we get the simple quadratic expression

$$\langle p^{(2)}\rangle_\Delta = -\frac{2}{\pi^3}\sum_{n=0}^{\infty} \frac{\sin\left((2n+1)\pi z_0\right)}{(2n+1)^3} = -\frac{1}{4} z_0(1 - z_0)\ .$$

As shown in figures 6(a) and 6(b), the comparison between the results predicted by these formulae and those obtained numerically with an Euler solver (more on this in section 6 below) are very reasonable. Another comparison with the numerics is offered by figure 7. Here, for the hook configuration, the quadratic asymptotic scaling of $\langle p\rangle_\Delta \propto \rho_\Delta^2$ can be seen explicitly, with the theory providing an excellent fit for small values of ρ_Δ. The agreement persists up to fairly large values of ρ_Δ. A relative error of 10% is not reached until $\rho_\Delta \simeq 0.2$.

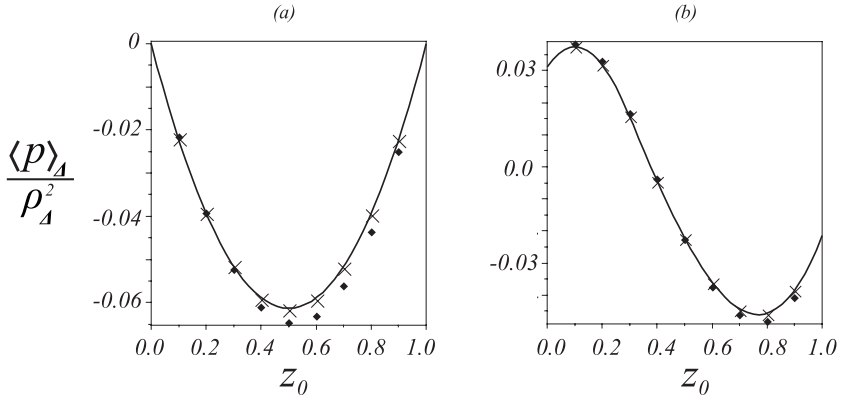

Figure 6: (a) Full hook case, with $A_2 - A_1 = A_3 - A_2 = 1.5$, $z_3 = z_0$, $z_1 = 0$, $z_2 = 1$, $\rho_\Delta = 0.01$ (crosses), $\rho_\Delta = 0.1$ (diamonds), from numerics (§6), theoretical value (solid line) from asymptotics $\rho_\Delta \to 0$. (b) Kink-like case, with $A_2 - A_1 = A_3 - A_2 = 1.5$, $z_1 = 0.3$, $z_2 = 0.8$, $z_3 = 0.5$, $\rho_\Delta = 0.01$ (crosses), $\rho_\Delta = 0.1$ (diamonds), from numerics (§6), theoretical value (solid line) from asymptotics $\rho_\Delta \to 0$ (equation (71)).

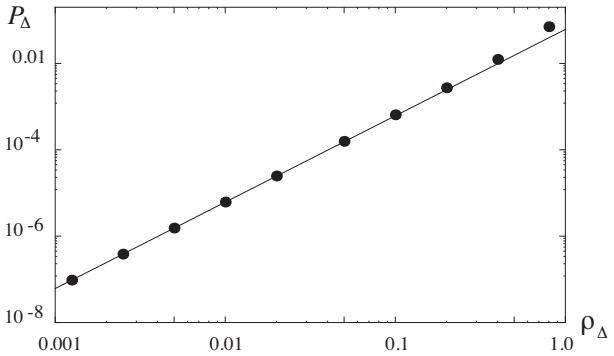

Figure 7: Pressure imbalance P_Δ vs. density difference ρ_Δ. Theory (solid line) from equation (71) and VARDEN simulation (dots). The interface is a "hook" (figure 5) with parameters given by $z_0 = z_3 = 0.5$, $z_1 = 1$, $z_2 = 0$, and $A_2 - A_1 = A_3 - A_2 = 1.5$ as in figure 6(a). The 2:1 slope is maintained up to density differences as large as $\rho_\Delta \simeq 0.2$ (in units of ρ_2).

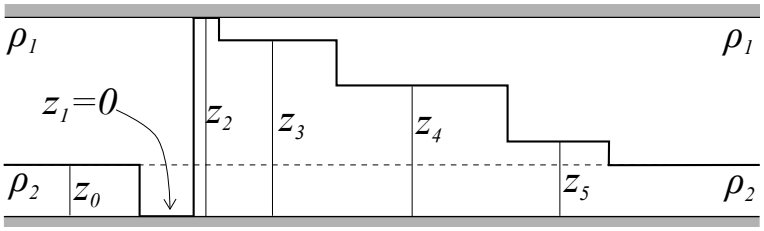

Figure 8: The special configuration of a staircase hook for a two-fluid density distribution in an x-infinite channel between two rigid plates located at $z = 0, 1$.

In general, in the limit $(A_{i+1} - A_i)$ large (as compared with the height of the channel), the Fourier series of (66) can be easily summed. Indeed, in this case the expression of the pressure jump reduces to

$$\langle p^{(2)} \rangle_\Delta = \left(\sum_{\alpha=1}^{N} \sum_{k=1}^{\infty} \frac{1}{\pi^3 k^3} (\sin(k\pi(z_\alpha - z_{\alpha-1})) + \frac{1}{2} \sum_{k=1}^{\infty} \frac{1}{\pi^3 k^3} \left(\sin(2k\pi z_0) - \sin(2k\pi z_n)\right) \right),$$

which yields

$$\langle p^{(2)} \rangle_\Delta = \left(\sum_{\alpha=1}^{N} \mathrm{sgn}(z_\alpha - z_{\alpha-1}) \mathcal{Q}_1(|z_\alpha - z_{\alpha-1}|) + \mathcal{Q}_2(z_0) - \mathcal{Q}_2(z_N) \right), \tag{72}$$

where $\mathcal{Q}_1$ and $\mathcal{Q}_2$ are the polynomials (see, e.g., Gradshteyn et al., 2000)

$$\begin{aligned} \mathcal{Q}_1(x) &= \frac{1}{12}x^3 - \frac{1}{4}x^2 + \frac{1}{6}x = \frac{1}{12}x(x-1)(x-2) \\ \mathcal{Q}_2(x) &= \frac{1}{3}x^3 - \frac{1}{2}x^2 + \frac{1}{6}x = \frac{1}{3}x(x-1)\Big(x - \frac{1}{2}\Big). \end{aligned} \tag{73}$$

It is interesting to note that even for a piecewise constant interfacial profile a qualitative agreement with the long-wave model result (48) can be detected. For the configuration depicted in figure 4, with an upward tooth of height A followed by a downward tooth of height B, equation (70) shows exponential decay of the pressure imbalance with increasing separation of the teeth. Further, the leading order behaviour is cubic in the heights A and B, and both expressions (48) and (70) are independent of rigid z-translations of the profile, for as long as the profile does not hit the channel's boundaries.

4.4 Special initial conditions: linear interfaces

We next consider the problem of the maximal $\langle p \rangle_\Delta$ with respect to special configurations. An interesting example is the "crooked hook" configuration depicted in figure 8: with the asymptotic heights at $z = z_0$, the first jump is to $z_1 = 0$, the second is to $z_2 = 1$, followed by a sequence of "steps" of heights

$$z_3 \geq z_4 \geq \cdots z_N = z_0 \,.$$

We assume $\min(A_{i+1} - A_i) \gg 1$, so that we can safely use formula (72) to determine the pressure jump as a function of the decreasing heights $z_3, z_4, \ldots, z_0$. The outcome is that the configuration maximizing $|\langle p^{(2)} \rangle_\Delta|$ is that of the left-hand side of the "crooked hook" being a well-crafted staircase, with steps of equal heights (e.g., in the figure, for $N = 5$ we have $z_0 = 1/5, z_3 = 4/5, z_4 = 3/5, z_5 = 2/5$). The sequence of the values of $\langle p^{(2)} \rangle_\Delta$ as N varies can be shown to admit $\langle p^{(2)} \rangle_\Delta = -\frac{1}{6}$ as the asymptotic value (as $N \to \infty$).

Other cases where the computations can be easily performed are those of piecewise linear profiles. For instance, let us consider the case of the "incline hook" as in figure 9, that is, a configuration of a jump located at $x = 0$, followed by a constant (negative) slope connecting the top of the step to the asymptotic height $z = z_0$.

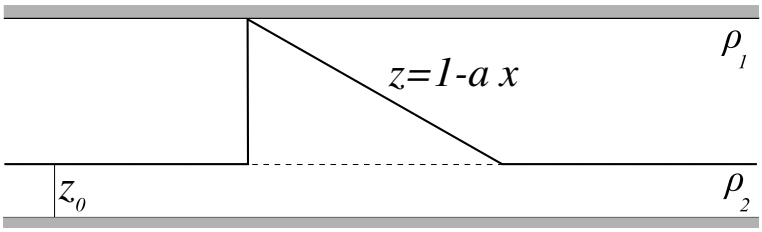

Figure 9: The "incline hook" configuration for a two-fluid density distribution in an x-infinite channel between two rigid plates located at $z = 0, 1$.

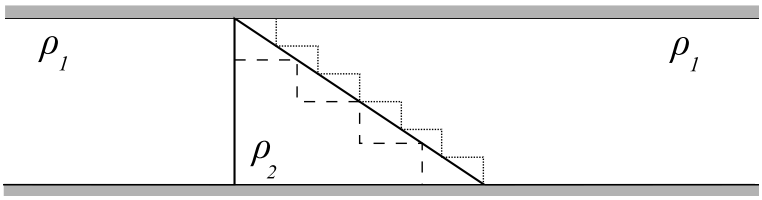

Figure 10: The piecewise constant vs. linear configurations for a two-fluid density distribution in an x-infinite channel between two rigid plates located at $z = 0, 1$.

From formula (64), the quantity $\langle p^{(2)} \rangle_\Delta$ is the sum of two terms, one given by the jump at $x = 0$, and the other given by the slope of the incline. Performing the integration, we get

$$\langle p^{(2)} \rangle_\Delta = \sum_{k=1}^{\infty} \left(\frac{\Phi_3 a^3 + \Phi_2 a^2 + \Phi_1 a + \Phi_0}{k^3 \pi^3 \left(1 + a^2\right)^2} \right), \tag{74}$$

with

$$\begin{aligned} \Phi_3 &= \left(1 + (-1)^k \cos\left(k\pi\, z_0\right)\right) \left(e^{k\pi\,(z_0-1)/a} - 1\right) \\ \Phi_2 &= k\pi(z_0 - 1) - (-1)^k \sin(k\pi z_0) \left(1 + 2\, e^{k\pi\,(z_0-1)/a}\right) \\ \Phi_1 &= -\left(1 - (-1)^k \cos\left(k\pi\, z_0\right)\right) \left(1 + e^{k\pi\,(z_0-1)/a}\right) \\ \Phi_0 &= k\pi(z_0 - 1) - (-1)^k \sin(k\pi z_0). \end{aligned} \tag{75}$$

In the limit $a \to 0, z_0 \to 0$, the series (74) reduces to

$$-\sum_{k=1}^{\infty} \frac{1}{\pi^2\, k^2} = -\frac{1}{6}.$$

This result matches the limiting value of the staircase of figure 8. Its interest lies in part on the fact that, although geometrically one would expect the limit of zero slope of the incline to yield a dam-break configuration, in which half of the channel is filled with "light" fluid and the remaining half is filled with "heavy" fluid, we see that the pressure differential is not given by the naïve geometrical limit. As computed exactly (for any density variation) in section 5 below, the dam-break configuration leads to zero pressure imbalance.

As a final example, we examine the pressure imbalances associated with sequences of staircase configurations with a fixed total width (see figure 10), with an increasing number of smaller and smaller steps. By using symbolic manipulators (Maple or Mathematica), it can be shown that the configuration that maximizes the pressure imbalance is that of the incline (solid line in figure 10), and that the limits from below and from above of the pressure imbalances of the piecewise constant staircases coincide with the pressure imbalance of their limiting linear profile. In this case the pressure imbalance agrees with the geometrical limit.

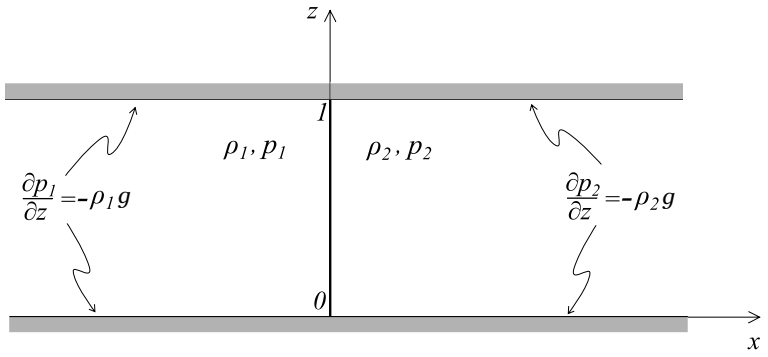

Figure 11: Dam-break configuration for a two-fluid density distribution. The pressure is everywhere continuous (and so, $\partial_z p_1 = \partial_z p_2$ at the interface $x = 0$) with the jump condition for its normal derivative at the interface $\partial_x p_1 = (\rho_1/\rho_2)\partial_x p_2$.

The above examples illustrate in a simple way how pressure imbalances can arise from localized variations of stratification, and how limiting processes can be affected by subtleties that require some care in order to be handled correctly. Next, we take a closer look at this issue in the context of an exact result, valid for any density difference, for the stratified Euler system.

5 Dam-breaking class

A nontrivial exact solution of equation (49), with the usual boundary conditions, can be obtained in the dam-break configuration depicted in figure 11: the heavier fluid (density ρ_2) fills the right side of the channel (assumed of height $h = 1$) and the rest of the channel (density ρ_1) is filled with the lighter fluid. The interface is therefore vertical, say at $x = 0$. In this case the asymptotic values of the interface are obviously different. By variable separation and solving by Fourier series, one finds closed-form expressions for pressure,

$$\begin{aligned} p_1 &= -\rho_1 g z - \rho_1 g \frac{\rho_\Delta}{\rho_1+\rho_2}\left(\frac{1}{2} - 4\sum_{n\,\text{odd}} \frac{1}{n^2\pi^2}\cos(n\pi z)e^{n\pi x}\right) \qquad \text{if } x \le 0 \\ p_2 &= -\rho_2 g z + \rho_2 g \frac{\rho_\Delta}{\rho_1+\rho_2}\left(\frac{1}{2} - 4\sum_{n\,\text{odd}} \frac{1}{n^2\pi^2}\cos(n\pi z)e^{-n\pi x}\right) \qquad \text{if } x \ge 0 \end{aligned} \tag{76}$$

where p_1 (p_2) is the pressure in the domain filled with the fluid with density ρ_1 (ρ_2). The pressure given in (76) is continuous in the whole channel, with a discontinuous x-derivative at $x = 0$. Moreover, this gradient has a (logarithmic) divergence at the points where the interface touches the boundaries. Indeed, it can be shown that

$$\frac{\partial p_1}{\partial x}\Big|_{x=0^-} = \frac{\rho_1\rho_\Delta g}{\pi(\rho_1+\rho_2)} \log\left(\frac{1+\cos(\pi z)}{1-\cos(\pi z)}\right).$$

One could expect that this configuration, due to the overall mass imbalance of the fluid, would consequently generate an overall pressure imbalance. However, this is not the case since for all $x \in \mathbb{R}$

$$\int_0^1 p_1(x,z,0)\,\mathrm{d}z \;= \int_0^1 p_2(x,z,0)\,\mathrm{d}z = -g\frac{\rho_1\rho_2}{\rho_1+\rho_2}. \tag{77}$$

Hence we have that $\langle p\rangle_\Delta = 0$ at $t = 0$. (Notice however that the numerical simulations presented in figure 13 show that a pressure imbalance will develop at times $t > 0$, so that the horizontal momentum is not conserved in the course of evolution.)

This example confirms that the nonconservation of the total horizontal momentum does not simply rely on the asymptotic difference of the purely hydrostatic pressure. In particular, we can interpret this result as an occurrence of another non trivial instance of boundary effects. In fact, let us consider a partial dam-break configuration, with the heavier fluid in the region $[0, +\infty) \times [0, z_1]$. One could expect it to generate a pressure difference which increases with the partial-dam height $z_1 \in [0, 1]$. However, as equation (77) shows, this is once again not the case, since the pressure differential for the dam-break limit ($z_1 = 1$) is null. This discontinuity might be regarded as a boundary effect, as suggested by the perturbative results of Section 4.3. Indeed, the expression for $\langle p^{(2)} \rangle_{\Delta}$ in this partial dam-break case, obtained by appropriate use of the polynomial formulae (72), yields $\langle p^{(2)} \rangle_{\Delta}(z_1) = (z_1^2 - z_1^3)/4$, whose minimum is at $z_1 = 2/3$.

Next, we remark that total horizontal momentum is always equal to that of the subsection of the channel spanned by the (maximal) horizontal support of the interface between the two fluids. In fact, volume conservation by incompressibility implies that at all times the volume flux vanishes,

$$\int_0^1 u(x, z, t) \mathrm{d}z = 0,$$

as this is satisfied as $|x| \to \infty$ (or at the lateral vertical walls for a finite channel). Since for homogeneous fluid the mass flux is simply proportional to the volume flux, the horizontal momentum for any channel's section of homogeneous fluid, i.e., sections that the "gravity currents" developing from the dam-break have not had time to reach, is zero. Further, the horizontal momentum of the fluid from a dam-break is directed towards the lighter fluid, since for computing horizontal momentum one needs to weigh the zero-volume-flux currents resulting from the dam-break with their different densities. The sign of pressure imbalance as it grows past the initial time can then be predicted to be opposite that of the momentum (i.e., positive when the denser fluid is to the right of the dam). This can also be seen intuitively from the center of mass time evolution (21). The two-fluid system admits a configuration of minimum potential energy corresponding to a flat interface, and it can be expected that the fluid's initial motion would be in the direction to achieve such configuration. Thus, the center of mass for a section between end points fully lying in regions of homogeneous fluids (where mass flux is zero), would move towards the lighter fluid, giving rise to a corresponding total horizontal momentum according to (21).

Let us now consider total vorticity evolution for the dam-break class. A general feature of the motion can be gleaned from (32). Taking into account that the interface is the segment $\{(0, z) \mid z \in [0, 1]\}$ and the density is given by $\rho = \rho_1 H(x) + \rho_2 H(-x)$ yields $\nabla p \times \nabla(1/\rho) = -\delta(x)\, p_z(0, z) \rho_{\Delta}/(\rho_1 \rho_2)$. Thus, from (32),

$$\begin{aligned} \Gamma_t^{\mathrm{dam}} &= \int_{\mathbb{R}\times[0,1]} \nabla p \times \nabla \left(\frac{1}{\rho} \right) \mathrm{d}A \\ &= -\int_{\mathbb{R}\times[0,1]} \frac{p_z(x, z) \rho_{\Delta}}{\rho_1 \rho_2} \delta(x) \, \mathrm{d}A = \frac{\rho_{\Delta}}{\rho_1 \rho_2} \left(p(0, 0) - p(0, 1) \right). \end{aligned} \tag{78}$$

The explicit solution (76) for the dam configuration implies

$$\Gamma_t^{\mathrm{dam}} = -\frac{2\rho_{\Delta}}{\rho_1 + \rho_2}. \tag{79}$$

We remark that this behaviour can be described as a boundary effect, by considering a limit in which the interface between the two fluids is made to coincide with one the boundaries of the channel (the lower for $x > 0$ and the upper for $x < 0$). Formula (37) can be used as depicted in figure 12, understanding the dam configuration as the limit of the full hook case when $A \to +\infty$, with A the length of the hook "teeth." In this limit the interface at $-\infty$ goes to 1 while at $+\infty$ it goes to 0. From (37) the time derivative of the total vorticity for the hook configuration is

$$\Gamma_t^{\mathrm{hook}} = \frac{\rho_{\Delta}}{\rho_1 \rho_2} \left[P_{\Delta} - (p(A, 0) - p(0, 0)) - (p(0, 1) - p(-A, 1)) \right]. \tag{80}$$

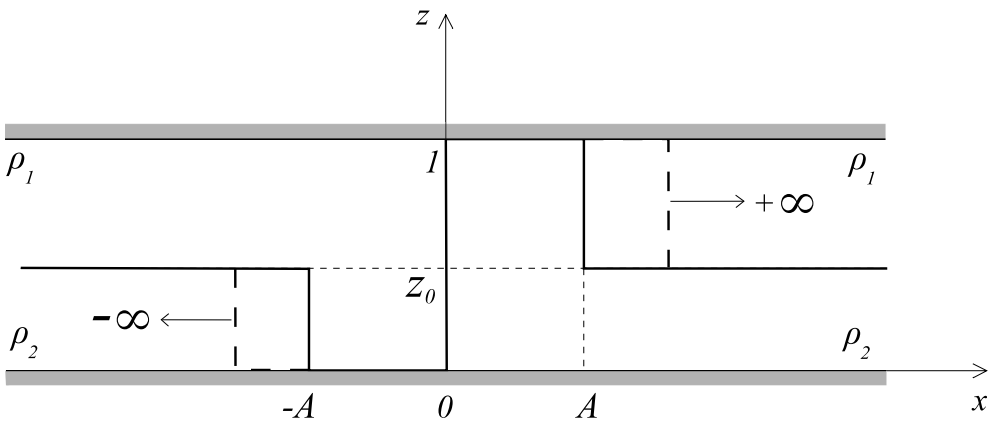

Figure 12: The geometric limit from the hook to dam configuration.

In the dam-break limit $A \to \infty$, $z_- \to 1$, and $z_+ \to 0$, where $P_\Delta = p(+\infty, 0) - p(-\infty, 1)$, we have

$$\begin{aligned}\Gamma_t^{\text{dam}} &= \lim_{A\to+\infty} \Gamma_t^{\text{hook}} \\ &= \frac{\rho_\Delta}{\rho_1\rho_2}\left[(p(+\infty,0) - p(-\infty,1)) - (p(+\infty,0) - p(0,0)) - (p(0,1) - p(-\infty,1))\right] \\ &= -\left(\frac{1}{\rho_1} - \frac{1}{\rho_2}\right)\left[p(0,1) - p(0,0)\right],\end{aligned} \tag{81}$$

which agrees with (78).

6 Time evolution: numerical results

We now focus on providing examples of the time evolution ensuing from the class of initial data we have analyzed. So far as we can see, this can only be done numerically. Of course, our analysis of inertia and incompressibility effects of the previous sections has been carried out with laterally unbounded domains in mind. For numerical investigations these infinite domains have to be truncated, for instance by erecting vertical no-flux walls. However, with rigid walls at the ends of sufficiently long channels, the inertia effects manifest in a similar way (for details, see Camassa et al. 2012). In the context of the theoretical examples studied in the previous sections, these inertia effects can be illustrated with direct numerical simulations of the time evolution of Euler equations in two dimensions. Our simulations are performed using the numerical algorithm VARDEN which solves the stratified incompressible Euler equations (see Almgren et al. 1998).

Details are as follows. The initial conditions in all our simulations (all performed using nondimensional quantities) are chosen among the specific cases discussed in Section 4 with zero initial velocities. The computation domain is $[-8, 8] \times [0, 1]$, and gravity is unity. We typically use a square grid of 512 points along the vertical, although we have run cases with doubled and half the resolution to assess convergence. For $t = 0$ results, two to three significant digits are kept as they are the same for all three resolutions. As fluid motion ensues, different resolutions show some discrepancies. However, the general density and velocity profiles as well as the important features in pressure jumps and total vorticity remain similar across resolutions.

6.1 Exact solutions: the dam problem

We begin our numerical simulations with the dam case, which is solved exactly in Section 5, and hence provides possibly the best test for numerical validation. We choose density parameters of the top and lower layers to be $\rho_1 = 0.9$ and $\rho_2 = 1.0$. Figure 13(a) shows the time evolution of $\langle p \rangle_\Delta$, from which we can see that $\langle p \rangle_\Delta = 0$ and $\partial_t \langle p \rangle_\Delta = 0$ at $t = 0$, validating our theoretical results (see also Appendix B). Here, as well as in figures 14

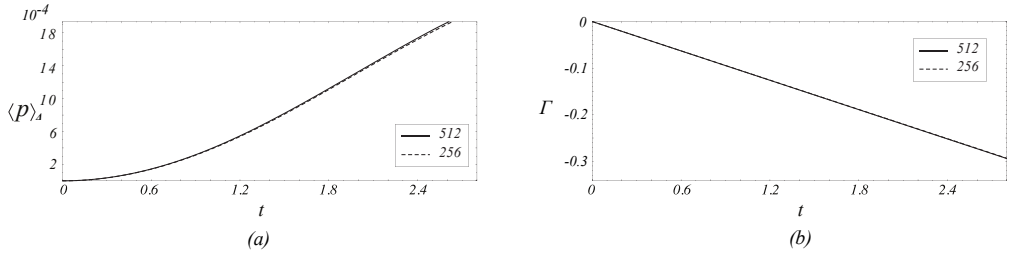

Figure 13: (a) Pressure jump and (b) total vorticity time history for the dam-break initial condition sketched in figure 11, in the time interval $0s < t < 2.8s$ with 512 (solid line) and 256 (dotted line) vertical points resolutions. The initial velocities of the fluids are zero, the fluid densities are $\rho_1 = .9$ and $\rho_2 = 1$ and the height of the channel is fixed to 1.

and 15, we perform numerical simulations with 256 and 512 vertical grid points, confirming that the time evolution is largely independent of resolutions. Figure 13(b) shows the total vorticity, exhibiting a linear behaviour of Γ near to $t = 0$, despite the fact that the pressure imbalance evolves from zero with zero slope. With the density parameters we have chosen in this section the value of the total vorticity obtained from this formula is $\Gamma_t^{\rm dam} = -1.05 \times 10^{-1}$. The value obtained from the numerical simulation related to figure 13(b) is $\Gamma_t^{\rm dam} = -1.05 \times 10^{-1}$ which agrees rather well with the theory. Snapshots of fluid time evolutions are shown in figure 16.

6.2 Asymptotic solutions: the hook case(s)

Our next example is the case of figure 5, in which $z_0 = z_3 = 0.5$, $z_1 = 0.1$, $z_2 = 0.9$, and $A_2 - A_1 = A_3 - A_2 = 1.5$. We choose density parameters of the top and lower layers to be $\rho_1 = 0.9$ and $\rho_2 = 1.0$ so that the case qualifies small ρ_Δ analysis discussed in Section 4.1. Figure 17 are snapshots of density profile up to time $t = 2.8$. Figures 14(a) and 14(b) show the pressure jump $\langle p \rangle_\Delta$ and the total vorticity Γ for $t = 0 \sim 2.8$. The pressure jump is -4.95×10^{-4} at $t = 0$, in reasonable quantitative agreement with equation (70), which predicts $\langle p \rangle_\Delta \sim \rho_\Delta^2 \langle p^{(2)} \rangle_\Delta = -4.72 \times 10^{-4}$. The total vorticity time derivative $\Gamma_t = -5.49 \times 10^{-5}$ also shows a good agreement with equation (37), by which $\Gamma_t \sim -5.25 \times 10^{-5}$. Since in this case the interface does not reach either the top or the bottom of the channel, the pressure difference between the interacting points x_i^L and x_i^R is neglected. When $t < 0.5$, the pressure jump is almost constant and the total vorticity behaves linearly, which can be explained by $\langle p \rangle_{\Delta t} = 0$ for $t = 0$ in case of zero initial velocities. Next we let $z_1 = 0$ and $z_2 = 1$, so that the interface touches the channel's boundary. Figure 18 shows the snapshots of density profile for time between 0 and 2.8. At $t = 0$, the pressure jump (figure 15(a)) is -6.46×10^{-4} and the total vorticity time derivative (figure 15(b)) is 2.80×10^{-5}. Equations (70) and (37) provide $\langle p \rangle_\Delta \sim -6.13 \times 10^{-4}$ and $\Gamma_t \sim 2.82 \times 10^{-5}$. The error is consistent with a second order-ρ_Δ^2 estimate when $\rho_\Delta = 0.1$. From the figures it is apparent that, in both the full hook and in the hook with slivers, the pressure imbalance $\langle p \rangle_\Delta$ has initial zero time-derivative (this point is further taken on in Appendix B).

We remark that we limited the time of evolution in all our numerical simulations to relatively short times, in order to maintain reasonable accuracy. An example of convergence for our numerical simulations is depicted in figure 19. As can be seen, the difference of two resolutions, 256 and 512 in the vertical directions, in the density field is maximal within a thin layer around the interface of the two fluids, not unexpectedly due to slight differences in the interface position and the effects of numerical diffusivity.

7 Conclusions

Total momentum conservation in the time-evolution of a stratified, incompressible ideal fluid is subject to a subtle interplay among boundary forces, incompressibility and inertia linked to the spatial extent of the

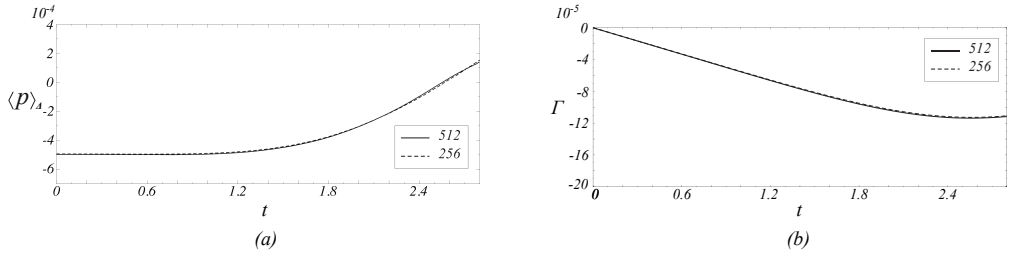

Figure 14: (a) Same as figure 13 but for the "hook with sliver" initial condition (figure 5) with $z_0 = z_3 = 0.5$, $z_1 = 0.1$ and $z_2 = 0.9$.

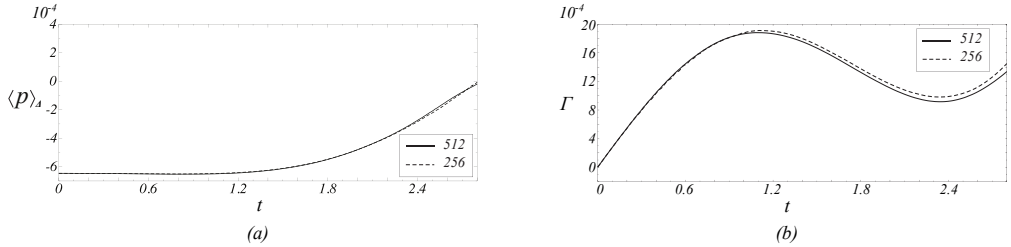

Figure 15: (a) Same as figure 13 but for "complete hook" initial condition (figure 5) with $z_0 = z_3 = 0.5$, $z_1 = 0$ and $z_2 = 1$.

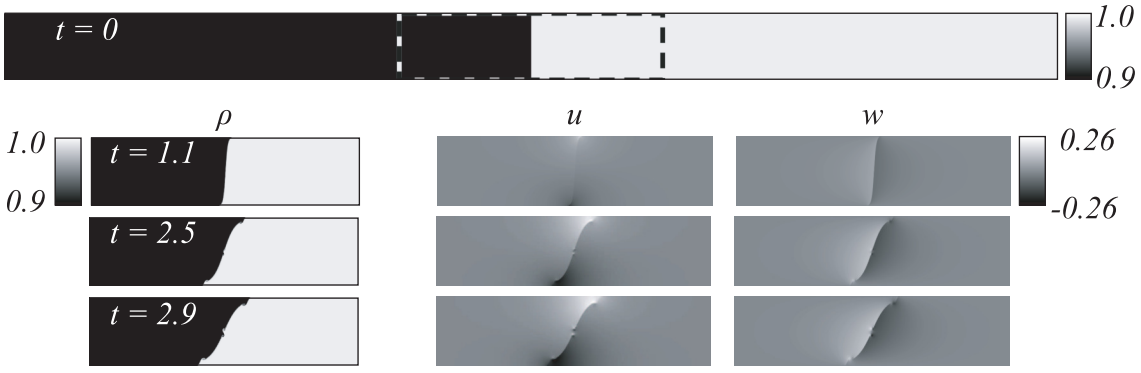

Figure 16: Snapshots of density ρ and velocities (u, w) (for horizontal and vertical component, respectively) for the time evolution of motion with the dam-breaking initial condition sketched in figure 11. Resolution is 512 vertical points, with physical parameters for this computation listed in the caption of figure 13. The initial density configuration is depicted in the top panel, which also illustrates the actual computational domain and its aspect ratio, while the subdomain for the snapshots is highlighted by a dashed contour.

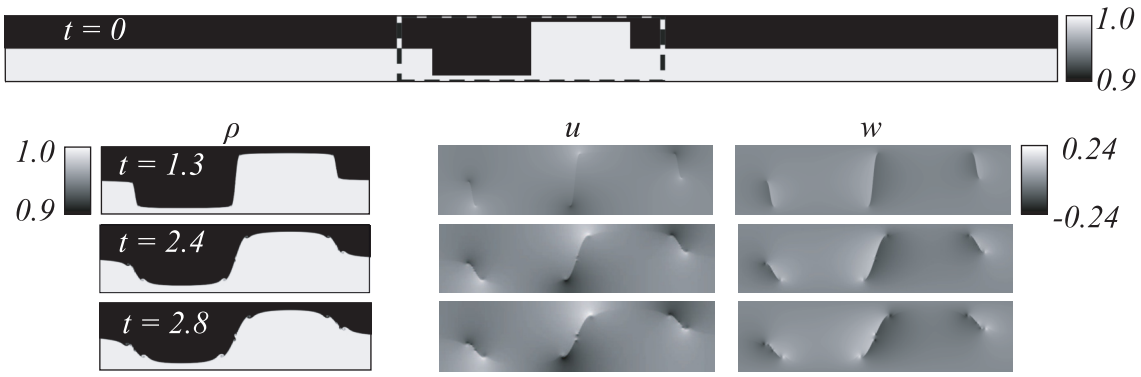

Figure 17: Same as figure 16 but for the "hook with sliver" initial condition case (figure 5). Physical parameters listed in caption of figure 14.

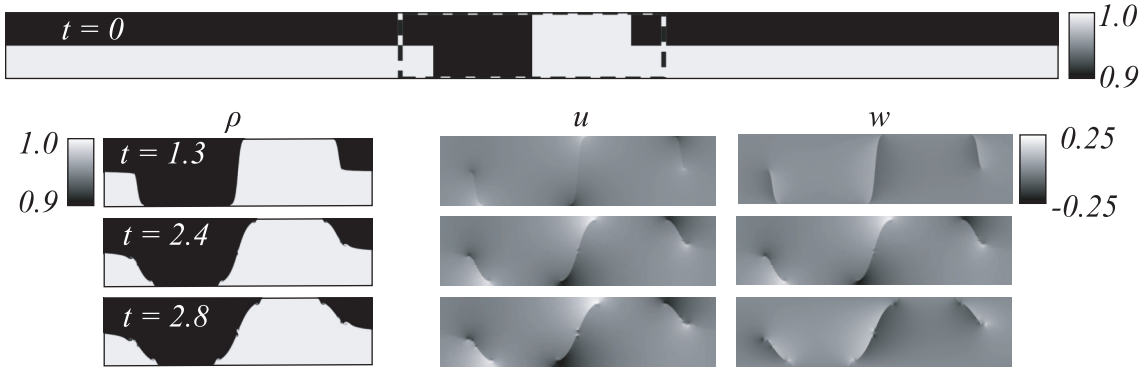

Figure 18: Same as figure 16 but for the "complete-hook" initial condition case (figure 5). Physical parameters listed in caption of figure 15.

Figure 19: Convergence of numerical algorithm for the "hook with sliver" initial data. Plotted here is the density difference at $t = 2.8$, generated by subtracting off the density from computations with 512 and 256 (vertical) nodes. Only the central portion (1/3 of the total length) of the channel is shown. For initial conditions that do not smooth the density jump, the resolution error becomes noticeable along the interface, where slight differences in its position in addition to numerical diffusion lead to nonzero density differences between the two computations.

fluid's domain. The case of an inhomogeneous, laterally infinite fluid confined between two-horizontal rigid plates offers perhaps the simplest set-up to illustrate this interplay, as we have shown directly from the motion equations in Camassa et al. (2012), and remarked by Benjamin (1986) in his study of Hamiltonian invariants. General formulae established by either approach suggest that horizontal momentum can fail to be conserved, even though only forces along the vertical direction act on such systems. These formulae connect momentum conservation to the pressure imbalance in the far field dynamics of the fluid, with the dynamics evolving from localized initial data and hydrostatic equilibrium enforced at infinity. While general plausibility arguments, together with long-wave model calculations and direct numerical simulations, certainly make a convincing case for the validity of the conclusions in the above studies, an explicit computation of such pressure imbalances has so far been lacking. In the present study we fill this gap by providing explicit examples.

Specifically, we have presented a systematic study of classes of initial data which allow closed-form expressions for pressure imbalances to be derived. In particular, we have examined in detail the case of zero initial velocities and two-fluid systems, showing that in this case the nonlocal pressure component arising from localized density displacements is the result of a Neumann-to-Dirichlet boundary map. In the limit of small density differences such map can be computed asymptotically, revealing non-intuitive properties of limiting configurations with simple piecewise constant initial conditions. (A similar analysis can be performed in the opposite limit $\rho_1 \to 0$, akin to an "air-water" system whenever air can be viewed as approximately incompressible, and will be studied in future publications). In particular, an exact expression shows that an internal "dam-breaking" problem, which leads to evolution of internal gravity currents, initially evolves maintaining constant horizontal momentum, as the total pressure imbalance is zero for such configuration.

Throughout our study, the long-wave models, and in particular the strongly nonlinear dispersive terms, have provided intuition, while correctly predicting scalings and parametric dependences for pressure imbalances for all the cases we have examined. Remarkably, qualitative and partially quantitative agreement continued to hold even when non-smooth data violated the asymptotic assumption that lay at these models' foundation. To this end, we have treated the technical point arising in connection with distributional derivatives due to density and velocity jumps. We have further shown how global-vorticity balance-laws for the class of initial data we have studied relate to pressure imbalances.

Lastly, in Appendix A we briefly discuss how our set-up can be framed within known variational principles. This allows a compact formulation of conservation laws through invariance under symmetry and Noether's theorem.

It is worth stressing again that in this study we have focussed on providing explicit expressions for the initial conditions we have examined. More general results along these lines of investigation properly pertain to mathematical analysis of general elliptic problems, and in particular to their Neumann-to-Dirichlet operators. These go beyond a fluid mechanical perspective, though nonetheless worth pursuing in future studies.

Acknowledgments

We thank R. Pego for discussions about conservation laws and Hamiltonian formalism, V.E. Zakharov for discussions about the Hamiltonian approach to the theory of non-homogeneous fluids, and A. Russo for discussions about numerical solutions of the Laplace equations with non-regular boundary conditions. Partial support by NSF grants DMS-0509423, DMS-1009750, RTG DMS-0943851 and CMG ARC-1025523, as well as by the MIUR Cofin2008 project *Geometrical Methods in the Theory of Nonlinear Waves and Applications* is acknowledged. R.C., S.C. and M.P. would like to thank the *Dipartimento di Matematica e Applicazioni* of the Milano-Bicocca University for its hospitality. Last, but not least, we would like to thank the anonymous referees whose attentive reading of the manuscript greatly helped improve the exposition of the first draft.

A Translational invariance and symmetries

In this appendix we discuss the translational invariance of the system. Indeed, regardless of the kind of constraint represented by the lids, translation along the horizontal axis is a symmetry of the system, so that a conservation law should ensue, as already clearly pointed out by Benjamin (1986). However, this conserved quantity for motion between two rigid lids does *not* correspond to the horizontal component of momentum, as is usually the case in unconstrained dynamics; instead it includes a contribution from boundary terms, as we briefly summarize below. To tackle these issues, we review the Lagrangian and Hamiltonian formulation of the governing equation (1) for a heterogeneous fluid. It is fair to say that the results of this appendix can be derived from those in the referenced literature. However, it is useful to collect them here for self-consistency and ease of reference.

As well known, the Euler system (1) admits a variational formulation. We focus first on the Lagrangian approach, following Zakharov et al. (1985) and Zakharov & Kuznetsov (1997). The basic idea is to use a subset of the Euler equations as constraints in the Lagrangian. Thus, the action is written with the usual difference between kinetic and potential energy, plus terms with Lagrange multiplier for constraints,

$$\begin{aligned} A &\equiv \int_{t_0}^{t_1} L \mathrm{d}t \\ &= \int_{t_0}^{t_1} \left(\frac{1}{2} \int_{\mathcal{D}} \rho |\mathbf{v}|^2 \, \mathrm{d}V - \int_{\mathcal{D}} \rho g z \, \mathrm{d}V + \int_{\mathcal{D}} \Phi \nabla \cdot \mathbf{v} \, \mathrm{d}V - \int_{\mathcal{D}} \lambda (\rho_t + (\mathbf{v} \cdot \nabla)\rho) \, \mathrm{d}V \right) \mathrm{d}t, \end{aligned} \tag{82}$$

where $\mathcal{D}$ is the fluid domain and $\mathrm{d}V$ its (two-dimensional) volume measure. By varying the action A with respect to all the fields entering L, we get the following equations

$$\begin{aligned} &\frac{\delta A}{\delta \Phi} = 0 \Rightarrow \nabla \cdot \mathbf{v} = 0 \,, \qquad \frac{\delta A}{\delta \lambda} = 0 \Rightarrow \rho_t + (\mathbf{v} \cdot \nabla)\rho = 0 \,, \\ &\frac{\delta A}{\delta \rho} = 0 \Rightarrow \lambda_t + \nabla \cdot (\lambda \mathbf{v}) + \frac{1}{2} |\mathbf{v}|^2 - g\, z = 0, \end{aligned} \tag{83}$$

and, in particular, the defining relation

$$\frac{\delta A}{\delta \mathbf{v}} = 0 \Rightarrow \rho \mathbf{v} - \nabla \Phi - \lambda \nabla \rho = 0. \tag{84}$$

This set of equations (Zakharov & Kuznetsov 1997) can be considered to be equivalent to the Euler equations (1).

When the domain, as in our case, is the infinite strip $\mathcal{S} = \mathbb{R} \times [0, h]$, translation along the x-axis is a symmetry of the system, and Noether's (first) theorem yields a conservation law for the Euler equations. For a Lagrangian system in two spatial dimensions with N fields $(\varphi_1, \varphi_2, \ldots, \varphi_N)$, the expression for this conservation law is

$$\sum_{\alpha=1}^{N} \left(\frac{\partial}{\partial t} \Big(\frac{\partial L}{\partial \varphi_{\alpha,t}} \varphi_{\alpha,x} \Big) + \frac{\partial}{\partial x} \Big(\frac{\partial L}{\partial \varphi_{\alpha,x}} \varphi_{\alpha,x} - L \Big) + \frac{\partial}{\partial z} \Big(\frac{\partial L}{\partial \varphi_{\alpha,z}} \varphi_{\alpha,x} \Big) \right) = 0, \tag{85}$$

so that for the Lagrangian (82) we get

$$\frac{\partial}{\partial t}(\lambda \rho_x) + \nabla \cdot \mathbf{J} = 0, \quad \mathbf{J} = (-\Phi u_x + \lambda u \rho_x + \frac{1}{2} \rho |\mathbf{v}|^2 - \rho g z, -\Phi w_x + \lambda w \rho_x). \tag{86}$$

In order to properly identify the conserved quantity

$$\mathcal{I} = \int_{\mathcal{S}} \lambda \rho_x \, \mathrm{d}V \tag{87}$$

it is useful to cast the problem in the Hamiltonian formalism.

The Hamiltonian $H = T+U$ associated with the Lagrangian in (82) makes use of a pair of Clebsch variables (λ, Φ) (the Lagrange multipliers of the Lagrangian), and reads

$$H = \int_{\mathcal{S}} \left(\frac{1}{2}\rho|\mathbf{v}|^2 + g\rho\, z \right) \mathrm{d}V \quad \text{with } \mathbf{v} = (\lambda\nabla\rho + \nabla\Phi)/\rho.$$

It turns out that the equations of motion imply

$$\rho_t = \frac{\delta H}{\delta \lambda}\,, \qquad \lambda_t = -\frac{\delta H}{\delta \rho}\,,$$

that is, the density ρ and the Clebsch variable λ are canonically conjugate. We thus recover the conserved quantity (87), since, with respect to the canonical brackets, the functional generating translations along x is indeed $\mathcal{I}$.

To proceed further, we connect this formalism with the set-up of Benjamin (1986), which does not make use of the (implicitly defined) Clebsch variables. The basic variables here are the density ρ together with a kind of density-weighted vorticity σ defined by

$$\sigma = (\rho w)_x - (\rho u)_z. \tag{88}$$

The equations of motion for these two fields are

$$\begin{aligned} &\rho_t + u\rho_x + w\rho_z = 0 \\ &\sigma_t + u\sigma_x + w\sigma_z + \rho_x\big(gz - \tfrac{1}{2}(u^2+w^2)\big)_z + \tfrac{1}{2}\rho_z\big(u^2+w^2\big)_x = 0 \end{aligned} \tag{89}$$

They can be written in the form

$$\rho_t = -\left[\rho, \frac{\delta H}{\delta \sigma}\right], \qquad \sigma_t = -\left[\rho, \frac{\delta H}{\delta \rho}\right] - \left[\sigma, \frac{\delta H}{\delta \sigma}\right], \tag{90}$$

where, by definition, $[A, B] := A_x B_z - A_z B_x$, and

$$H = \int_{\mathcal{S}} \frac{1}{2}\rho\left(|\mathbf{v}|^2 + gz\right) \mathrm{d}V. \tag{91}$$

In turn, the Hamiltonian H is to be written in terms of the stream function ψ, which is related to Benjamin's variables (ρ, σ) via

$$\sigma = (\rho w)_x - (\rho u)_z = -(\rho\psi_x)_x - (\rho\psi_z)_z = -\rho\nabla^2\psi - \nabla\rho\cdot\nabla\psi. \tag{92}$$

As shown by Benjamin, equations (90) are actually a Hamiltonian system with respect to a non-canonical (actually, Lie algebraic) Hamiltonian structure, i.e., (89) can be written as

$$\rho_t = \{\rho, H\}_B, \qquad \sigma_t = \{\sigma, H\}_B$$

for the Poisson bracket that can be easily spelled out by (90).

A straightforward computation shows that the canonical (Zakharov 1985) and modified (Benjamin 1986) Hamiltonian structures are equivalent under the "coordinate transformation"

$$(\rho, \lambda) \to (\rho, \sigma) = (\rho, \lambda_x\rho_z - \lambda_z\rho_x), \tag{93}$$

where the equality $\sigma = \lambda_x\rho_z - \lambda_z\rho_x$ is a consequence of (84).

Benjamin's (1986) formalism is explicitly tailored for symmetries. The generator of translations along the horizontal directions (the "impulse") is, as it is easily verified,

$$\mathcal{I} = \int_{\mathcal{D}} z\sigma(x,z)\,\mathrm{d}V\,.$$

In particular, for two-dimensional motion between two rigid horizontal lids we have a bulk and boundary components,

$$\mathcal{I} = \int_{\mathcal{S}} \rho\, u \,\mathrm{d}V - \int_{\mathbb{R}} z\, \rho u|_{z=0}^{z=h} \,\mathrm{d}x,$$

where the first term in this sum is the ordinary total horizontal momentum, while the second term is a boundary term — called B_6 in Benjamin (1986). Indeed we have, in the infinite strip $\mathcal{S} = \mathbb{R} \times [0, h]$,

$$\begin{aligned} &\int_{\mathcal{S}} z\sigma \,\mathrm{d}V = \int_{\mathcal{S}} z(\rho w)_x \,\mathrm{d}V - \int_{\mathcal{S}} z(\rho u)_z \,\mathrm{d}V = \int_0^h \left(\int_{\mathbb{R}} (z\rho w)_x \,\mathrm{d}x \right) \mathrm{d}z - \int_{\mathbb{R}} \left(\int_0^h z(\rho u)_z \,\mathrm{d}z \right) \mathrm{d}x \\ &= \int_0^h z\rho w|_{x=-\infty}^{x=+\infty} \,\mathrm{d}z - \int_{\mathbb{R}} z\rho u|_{z=0}^{z=h} \,\mathrm{d}x + \int_{\mathcal{S}} \rho u \,\mathrm{d}V = -\int_{\mathbb{R}} z\rho u|_{z=0}^{z=h} \,\mathrm{d}x + \int_{\mathcal{S}} \rho u \,\mathrm{d}V, \end{aligned} \tag{94}$$

thanks to the boundary conditions. This yields

$$\mathcal{I} + \int_{\mathbb{R}} z\rho u|_{z=0}^{z=h} \,\mathrm{d}x = \int_{\mathbb{R}\times[0,h]} \rho u \,\mathrm{d}V.$$

Using the Euler equation for the horizontal momentum (see (4))

$$(\rho u)_t = -\frac{1}{2}\rho_x(u^2 + w^2) - \left[\frac{1}{2}\rho(u^2 + w^2) + p \right]_x + w\,\sigma \tag{95}$$

at $z = h$ (where w vanishes) yields

$$(\rho u)_t = -\frac{1}{2}\rho_x(u^2) - \left[\frac{1}{2}\rho u^2 + p \right]_x,$$

and so

$$\frac{dB_6}{dt} = -h \left(\int_{\mathbb{R}} \frac{1}{2}\rho_x(u^2)|_{z=h} \mathrm{d}x + p(+\infty, h) - p(-\infty, h) \right). \tag{96}$$

In the case of constant density at the top lid, and with an equilibrium distribution $\rho_0 = \rho_0(z)$ (the case of Benjamin, 1986), this reduces to

$$\frac{dB_6}{dt} = -h \left(p(+\infty, h) - p(-\infty, h) \right).$$

Quoting Benjamin (1986):

> *"Here $p(+\infty, h)$ and $p(-\infty, h)$ are the pressure levels as $x = +\infty$ and $x = -\infty$ relative to hydrostatic pressure in the quiescent state of the whole system; and while only their difference can have any dynamic significance there is no reason in general for it to be zero or take any other constant value."*

In the bulk of the paper we have constructed solutions for which this pressure difference can be computed analytically. Here we have consistently recovered that the systems admits a conservation law corresponding to the x-translational invariance, but this quantity might not coincide (in general) with the x-component of the total momentum. Rather, the invariant is the sum of such a bulk term and of the boundary term B_6, whose time variation is given by the pressure imbalance of the system for $x \to \pm\infty$.

B Time derivative of $\langle p \rangle_{\Delta}$ at t = 0

The results of §4 in general hold only when the velocity $\mathbf{v}$ vanishes (the initial condition for all our numerical simulations). Here we consider the time derivative of $\langle p \rangle_{\Delta}$ and show how the behaviour of our numerical simulations for small (but nonzero) time can be framed within our theoretical set-up.

The continuity equation implies that if $\mathbf{v} = 0$ then $\rho_t = 0$. Differentiating the momentum equations with respect to time when $\mathbf{v} = 0$ yields

$$\mathbf{v}_{tt} + \frac{1}{\rho}\nabla p_t = 0. \tag{97}$$

From incompressibility of the fluid we have that

$$\nabla \cdot \left(\frac{1}{\rho}\nabla p_t\right) = 0. \tag{98}$$

Therefore p_t satisfies the same equation as p but with *homogeneous* boundary conditions. Indeed,

$$\frac{\partial p_t}{\partial x} \to 0 \quad \text{as} \quad |x| \to \infty\,, \qquad \frac{\partial p_t}{\partial z} = 0 \quad \text{at} \quad z = 0, h, \quad t = 0, \tag{99}$$

where we used again the fact that $\rho_t = 0$ when $\mathbf{v} = 0$. If ρ is smooth, Gauss theorem implies

$$0 = \int_{\mathbb{R}\times[0,h]} p_t \nabla \cdot \left(\frac{1}{\rho}\nabla p_t\right) \mathrm{d}x\,\mathrm{d}z = \int_{\mathbb{R}\times[0,h]} \frac{1}{\rho}|\nabla p_t|^2 \,\mathrm{d}x\,\mathrm{d}z\,, \tag{100}$$

where the last equality follows from the vanishing Neumann boundary conditions for p_t. Therefore $\nabla p_t = 0$ and in particular its first component p_{xt} vanishes. Hence

$$\partial_t \langle p \rangle_{\Delta} = \int_0^h p_t\Big|_{x=+\infty} \mathrm{d}z - \int_0^h p_t\Big|_{x=-\infty} \mathrm{d}z = \int_0^h \left(\int_{-\infty}^{+\infty} p_{xt}\,\mathrm{d}x\right) \mathrm{d}z = 0. \tag{101}$$

Thus, if at $t = 0$, the velocity data are $\mathbf{v} = 0$, then the time derivative of the pressure imbalance vanishes as well.

The presence of an interfacial discontinuity in the density requires some attention in applying Gauss theorem. For this, in analogy with what we have done in computing the time derivative of the total vorticity in §2, we have to break the integration domain according to figure 2. This contributes new boundary terms to the right hand side of (100), in the form of a net flux through the interface between the two fluids

$$\int_\gamma \frac{1}{\rho_1}\frac{\partial p_t}{\partial n_1}\,\mathrm{d}\sigma + \int_\gamma \frac{1}{\rho_2}\frac{\partial p_t}{\partial n_2}\,\mathrm{d}\sigma\,, \tag{102}$$

where n_1 (n_2) is the normal to the interface exterior to the domain of fluid with density ρ_1 (ρ_2), and integration is taken along the interface $\gamma = \{(x, \eta(x)) \mid x \in \mathbb{R}\}$. The boundary conditions on the interface given in (51) imply

$$\frac{1}{\rho_1}\frac{d}{dt}\frac{\partial p}{\partial n_1} = -\frac{1}{\rho_2}\frac{d}{dt}\frac{\partial p}{\partial n_2}\,, \tag{103}$$

because $n_2 = -n_1 \equiv n$. Note that the normal to the interface between the two fluids depends on time. However, when the velocity of the fluid is everywhere zero, the kinematic boundary condition reduces to $\eta_t = 0$, so that $n_t = 0$. Finally,

$$\frac{1}{\rho_1}\frac{\partial p_t}{\partial n_1} = -\frac{1}{\rho_2}\frac{\partial p_t}{\partial n_2}\,, \tag{104}$$

and therefore the new interface contribution (102) is identically zero. Thus, for the special case of vanishing velocity initial condition, $\partial_t \langle p \rangle_{\Delta} = 0$ at $t = 0$.

C Boundary effects in air water systems

For those configurations in which the interface of a two-layer fluid coincides somewhere with one of the channel upper or lower boundaries, the formulae previously computed may, in general, be incorrect and have to be appropriately modified. This is best appreciated by looking at specific examples, which we consider next. A deeper and more systematic analysis of this kind of phenomena would be outside of the aims of the present paper and will be reported separately. Here we limit ourselves to a brief discussion, by using the long-wave model, of how the combination of "air-water"-like stratification and boundary effects influence the pressure imbalance.

As previously remarked, in the long-wave (dispersionless) approximation, the pressure difference P_{Δ} is given by

$$P_{\Delta} = h \int_{-\infty}^{\infty} \frac{(\overline{u_1}\ \overline{u_2})_x}{\eta_2/\rho_2 + \eta_1/\rho_1}\, \mathrm{d}x. \tag{105}$$

If the interface is (sufficiently) far from the upper boundary (that is, if $\eta_2(x) = \eta(x) \neq h$ for all x), then P_{Δ}, for fixed ρ_2, goes to zero when ρ_1 goes to zero. However, the same conclusion cannot be drawn when the region occupied by the lighter fluid is disconnected.

In order to study this problem for $\rho_1 \to 0$, let us rewrite (105) as

$$P_{\Delta} = h \int_{\mathbb{R}/\mathcal{C}} \frac{(\overline{u_1}\ \overline{u_2})_x}{\eta_2/\rho_2 + \eta_1/\rho_1}\, \mathrm{d}x + h \int_{\mathcal{C}} \frac{(\overline{u_1}\ \overline{u_2})_x}{\eta_2/\rho_2 + \eta_1/\rho_1}\, \mathrm{d}x, \tag{106}$$

where $\mathcal{C}$ is the subset of $\mathbb{R}$ (which we can assume, for the sake of definiteness, to be the segment $\mathcal{C} = [x^L, x^R]$) where η_1 is sufficiently small in such a way that

$$\frac{\rho_1}{\eta_1} \simeq \frac{\rho_2}{\eta_2} \tag{107}$$

holds even if $\rho_1 \ll \rho_2$. In this case only the second integral contributes to the pressure imbalance P_{Δ}. If we consider the double scaling limit $\rho_1/\eta_1 \simeq \rho_2/\eta_2$ for $\rho_1 \to 0$ and $\eta_1 \to 0$ (and therefore $\mathcal{C} = \{x \in \mathbb{R} \mid \eta_1(x) \leq h\rho_1/\rho_2\}$), then relation (106) becomes

$$P_{\Delta} = \rho_2 h \int_{\mathcal{C}} \frac{(\overline{u_1}\ \overline{u_2})_x}{2\eta_2}\, \mathrm{d}x \simeq \frac{\rho_2}{2} \overline{u_1}\ \overline{u_2}\Big|_{x^L}^{x^R}. \tag{108}$$

Hence, in this particular limit, there is no reason for P_{Δ} to vanish when ρ_1 goes to zero.

We finally mention that a similar qualitative result can be obtained in the case of zero initial velocities, provided that the dispersive terms of (45) be included in the calculation of P_{Δ}. In the same approximations of the dispersionless case we obtain the estimate

$$P_{\Delta} \sim -\frac{g\rho_2 h^2}{12} \eta_{2xx}\Big|_{x^L}^{x^R}. \tag{109}$$

References

[Almgren et al. (1998)] Almgren, A.S., Bell, J.B., Colella, P., Howell, L.H. & Welcome, M.L. 1998 A conservative adaptive projection method for the variable density incompressible Navier-Stokes equations. *J. Comput. Phys.*, **142**, 1–46.

[Baines (1995)] Baines, P.G. *Topographic Effects in Stratified Flows.* Cambridge University Press, Cambridge, 1995.

[Benjamin (1986)] Benjamin, T.B. 1986 On the Boussinesq model for two-dimensional wave motions in heterogeneous fluids. *J. Fluid Mech.*, **165**, 445–474.

[Boonkasame & Milewski (2011)] Boonkasame, A. & Milewski, P. 2012 The stability of large-amplitude shallow interfacial non-Boussinesq flows. *Stud. Appl. Math.*, **128**, 40–58.

[Camassa et al. (2012)] Camassa, R., Chen, S., Falqui, G., Ortenzi, G. & Pedroni, M. 2012 An inertia 'paradox' for incompressible stratified Euler fluids. *J. Fluid Mech.*, **695**, 330–240.

[Camassa et al. (2011)] Camassa, R., Choi, W., Michallet, H., Rusås, P.-O. & Sveen, J.K. 2006 On the realm of validity of strongly nonlinear asymptotic approximations for internal waves. *J. Fluid Mech.*, **549**, 1–23.

[Camassa & Levermore (1997)] Camassa, R. & Levermore, C.D. 1997 Layer-mean quantities, local conservation laws, and vorticity. *Phys. Rev. Lett.*, **78**, 650–653.

[Camassa & Tiron (2011)] Camassa, R. & Tiron, R. 2011 Optimal two-layer approximation for continuous density stratification. *J. Fluid Mech.*, **669**, 32–54.

[Choi & Camassa (1999)] Choi, W. & Camassa, R. 1999 Fully nonlinear internal waves in a two-fluid system. *J. Fluid Mech.*, **396**, 1–36.

[Esler & Pearce (2011)] Esler, J.G. & Pearce, J.D. 2011 Dispersive dam-break and lock-exchange flows in a two-layer fluid. *J. Fluid Mech.*, **667**, 555–585.

[Gelfand & Shilov (1964)] Gelfand, I.M & Shilov, G.E. *Generalized Functions* Academic Press, New York, 1964.

[Gradshteyn et al. (2000)] Gradshteyn, I.S, Ryzhik, I.M., Jeffrey, A. & Zwillinger, D. *Tables of integrals, Series, and Products*. Academic Press, New York, 2000.

[Milewski et al. (2004)] Milewski, P., Tabak, E., Turner, C., Rosales, R.R. & Mezanque, F. 2004 Nonlinear stability of two-layer flows. *Comm. Math. Sci.*, **2**, 427–442.

[Wu (1981)] Wu, T.Y. 1981 Long waves in ocean and coastal waters. *J. of Eng. Mech.*, **107**, 501–522.

[Yih (1980)] Yih, C. *Stratified Flows*. Academic Press, New York, 1980.

[Zakharov & Kuznetsov (1997)] Zakharov, V.E. & Kuznetsov, E.A. 1997 Hamiltonian formalism for nonlinear waves. *Phys. Usp.*, **40**, 1087–1116.

[Zakharov et. al. (1985)] Zakharov, V.E., Musher, S.L. & Rubenchik, A.M. 1985 Hamiltonian approach to the description of non-linear plasma phenomena. *Phys. Rep.* **C**, 285–366.